

# The characteristics of atmospheric boundary layer height over the Arctic Ocean during MOSAiC

Shijie Peng<sup>1</sup>, Qinghua Yang<sup>1</sup>, Matthew D. Shupe<sup>2,3</sup>,

Xingya Xi<sup>1</sup>, Bo Han<sup>1</sup>, Dake Chen<sup>1</sup>, Sandro Dahlke<sup>4</sup>, Changwei Liu<sup>1\*</sup>

<sup>1</sup> School of Atmospheric Sciences, Sun Yat-sen University, and Southern Marine Science and Engineering Guangdong Laboratory (Zhuhai), Zhuhai 519082, China

<sup>2</sup> Cooperative Institute for Research in Environmental Sciences, University of Colorado Boulder, Boulder, CO, USA

<sup>3</sup> NOAA Physical Science Laboratory, Boulder, CO, USA

<sup>4</sup> Helmholtz Centre for Polar and Marine Research, Alfred Wegener Institute (AWI), Potsdam, Germany

Correspondence to: Changwei Liu (liuchw8@mail.sysu.edu.cn)

## Abstract

The important roles of the atmospheric boundary layer (ABL) in the central Arctic climate system have been recognized, but the atmospheric boundary-layer height (ABLH), defined as the layer of continuous turbulence adjacent to the surface, has rarely been investigated. Using a year-round radiosonde dataset during the Multidisciplinary drifting Observatory for the Study of Arctic Climate (MOSAiC), we improve a Richardson-number-based algorithm that takes cloud effects into consideration, and analyze the characteristics and variability of ABLH over the Arctic Ocean. The results reveal that the annual cycle is clearly characterized by a distinct peak in May and two minima in January and July. This annual variation in ABLH is primarily controlled by the evolution of ABL thermal structure. Temperature inversions in the winter and summer are intensified by seasonal radiative cooling and [warm air advection with surface temperature constrained by melting](#), respectively, leading to the low ABLH at these times. [Meteorological and turbulence variables also play a significant role in ABLH variation, including near-surface potential temperature gradient, friction velocity, and TKE dissipation rate](#). In addition, the MOSAiC ABLH is more suppressed than the ABLH during the Surface Heat Budget of the Arctic Ocean (SHEBA) experiment in the summer, which indicates that there is large variability in the Arctic ABL structure during summer melting season.

## 1 Introduction

In recent years, the rapidly changing climate and declining sea ice in the Arctic have been reported by numerous studies (e.g., Matveeva and Semenov, 2022; Meier and Stroeve, 2022; Esau et al., 2023). The Arctic near-surface temperature is increasing at a rate 2–3 times larger than the global average, which is referred to as Arctic amplification (Overland et al., 2019; Blunden and Arndt, 2019), and the Arctic has entered the ‘new Arctic’ period (Landrum and Holland, 2020). As a key component of the Arctic climate system, the atmospheric boundary layer (ABL) over the Arctic Ocean is closely associated with Arctic warming and has a big impact on sea ice loss (Francis and Hunter, 2006; Graversen et al., 2008; Wetzell and Bruemmer, 2011). Thus, it is critical to improve our understanding of Arctic ABL processes under ‘new Arctic’ conditions.

39 The ABL structure over the Arctic Ocean has unique characteristics due to the presence of semipermanent  
40 sea ice, and is shaped by various mechanisms including interactions with the surface, free atmosphere, and  
41 wave activity. Most studies of the Arctic ABL structure have been based on coastal observatories and limited  
42 drifting ice stations (Knudsen et al., 2018; Vullers et al., 2021). It has been found that a predominant  
43 temperature inversion in the lower troposphere exists in all seasons and is referred to as the “Arctic inversion”  
44 (Andreas et al., 2000; Tjernström et al., 2009). The Arctic inversion is sometimes elevated, with regions of  
45 near-neutral stability below the inversion (Persson et al., 2002; Tjernström et al., 2012). The Arctic vertical  
46 structure is influenced by many factors, such as warm-air advection, surface melt, cloud-top cooling, and  
47 turbulent mixing (Busch et al., 1982; Vihma et al., 2011; Vihma, 2014). Investigations of the ABL structure  
48 evolution and its controlling factors are the keys to knowing the ABL's role in the Arctic atmosphere (Sterk  
49 et al., 2014).

50 The atmospheric boundary-layer height (ABLH), here defined as the height of continuous turbulent  
51 mixing extending up from the surface, is the key indicator of the ABL structure (Seibert et al., 2000; Seidel  
52 et al., 2012). It determines the vertical extent of many atmospheric processes, such as convective transport  
53 and aerosol distributions, and is an important parameter for weather and climate models (Holtslag et al.,  
54 2013; Mahrt, 2014; Davy and Esau, 2016). In some previous studies, the ABLH over the Arctic Ocean is  
55 defined as the height of the surfaced-based inversion top or the capping inversion base (e.g., Tjernström et  
56 al., 2009; Sotiropoulou et al., 2014). However, as the most fundamental characteristic of the ABL, turbulence  
57 is not fully considered in this definition. There are two primary layers of turbulent mixing in the Arctic  
58 atmosphere. First, the surface layer, formed by turbulent mixing processes near the surface, is frequently  
59 shallower than the Arctic inversion layer (Mahrt, 1981; Andreas et al., 2000). Second, the turbulence  
60 associated with low-level clouds, which is driven by radiative cooling near the cloud top, forms a cloud-  
61 induced mixed layer (Solomon et al., 2011; Shupe et al., 2013). This cloud-driven mixed layer is sometimes  
62 decoupled from the surface mixed layer while at other times it extends down to form a coupled, well-mixed  
63 layer all the way to the surface (Shupe et al., 2013; Brooks et al., 2017). Wind-shear induced turbulence can  
64 also play a role in both of these layers and their interactions. Based on different turbulence characteristics,  
65 the ABLH is commonly determined using profiles of potential temperature, wind speed, and humidity, and  
66 various methods have been proposed for calculating ABLH (Seibert et al., 2000; Seidel et al., 2010).  
67 However, the applicability of these methods in the Arctic needs to be further assessed.

68 Due to the lack of observations, there are few analyses of ABLH over the Arctic Ocean based on  
69 observational data. Distributions of Arctic ABLH have been investigated by Tjernström and Graverson  
70 (2009), Liu and Liang (2010), and Dai et al. (2011), but their studies are all based on the Surface Heat Budget  
71 of the Arctic Ocean (SHEBA) campaign conducted 25 years ago (Uttal et al., 2002). To improve our  
72 understanding of the ABL structure and ABLH characteristics under “new Arctic” conditions, we need new,  
73 comprehensive observations in this environment. The Multidisciplinary drifting Observatory for the Study  
74 of Arctic Climate (MOSAIC) expedition was, in part, designed to achieve this goal (Shupe et al., 2022).  
75 Based on and around a drifting research vessel in the central Arctic for a whole year, the MOSAIC expedition  
76 provided a wealth of data and related data products with unprecedented high temporal resolution and year-

77 round temporal coverage. These data make possible a more detailed analysis of the ABL structure evolution  
78 and ABLH variability.

79 In this study, based on observational data from the MOSAiC expedition, we propose an improved ABLH  
80 algorithm and then examine the characteristics of the ABL evolution over the ‘new Arctic’ sea-ice surface.  
81 This paper is organized as follows: Section 2 briefly describes the MOSAiC expedition and the observations;  
82 section 3 provides an ABLH determination method to evaluate several automated algorithms, and develops  
83 an improved ABLH algorithm; section 4 presents the results of ABLH variation over the annual cycle, the  
84 controlling factors of ABLH variation, and mechanisms of ABL development and suppression; section 5  
85 compares the difference in ABLHs between SHEBA and MOSAiC; and conclusions are given in section 6.

86

## 87 **2 Measurements**

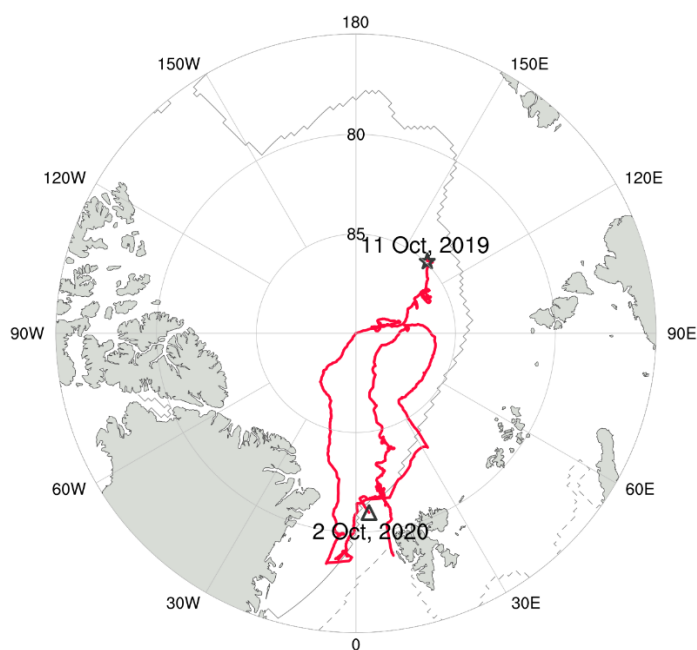
88 In this study, the SHEBA-based sounding data (Moritz, 2017) and multiple MOSAiC data are used. Here  
89 we mainly introduce the MOSAiC expedition. The MOSAiC track is shown in Fig. 1, which is based on the  
90 research vessel *Polarstern* (Knust, 2017), with the main period of atmospheric state observations starting in  
91 October 2019 and ending in September 2020. *Polarstern* drifted across the central Arctic Ocean and  
92 navigated through the sea ice north of 78° N during most of the MOSAiC year. The whole drifting period is  
93 divided into five parts, and the vessel sailed in the gap period between some of those parts. More details are  
94 provided in Shupe et al. (2022). The following are the descriptions of the instruments and data products used  
95 in this paper.

96

### 97 **2.1 Radiosonde observations and relevant data products**

98 The radiosonde data were obtained through a partnership between the leading Alfred Wegener Institute  
99 (AWI), the atmospheric radiation measurement (ARM) user facility, a US Department of Energy facility  
100 managed by the Biological and Environmental Research Program, and the German Weather Service (DWD)  
101 (Maturilli et al., 2022). Vaisala RS41-SGP Radiosondes were regularly launched on board throughout the  
102 whole MOSAiC year (from October 2019 to September 2020), including periods when the vessel was in  
103 transit. The sounding frequency is normally four times per day (launched at about 5:00, 11:00, 17:00, and  
104 23:00 UTC) and is increased to 7 times per day during periods of exceptional weather or coordination with  
105 other observing activities. The radiosoundings provide data on the atmospheric state, including vertical  
106 profiles of pressure, temperature, relative humidity (*RH*), and winds, from 12 m up to 30 km with a vertical  
107 resolution of 5 m. However, the sounding data below ~100 m altitude may be contaminated by the vessel  
108 itself. To avoid contamination affecting our analysis, we use a merged data product that combines the  
109 soundings with measurements from a meteorological tower on the sea ice away from the vessel, and was  
110 specifically designed to minimize ship effects and provide more reliable profiles in the lowest 100 m, which  
111 has been recently submitted (Dahlke et al., 2023). In this paper, data quality control and a six-point moving  
112 average in height are applied to the merged profile data to eliminate invalid data and measurement noise,  
113 and all data are interpolated onto a regular vertical grid with 10 m intervals. In total, there are 1484 sounding  
114 profiles available. In addition, DOE-ARM provides a Planetary Boundary Layer Height Value-Added

115 Product (PBLHT VAP, Riihimaki et al., 2019), which uses several different automated algorithms to compute  
116 ABLH estimates based on radiosonde profiles. This VAP provides 964 ABLH estimates, and we select 914  
117 samples from these to ensure that the estimates obtained by all algorithms are available.



118  
119 Figure 1 The MOSAiC expedition track from (star) 11 October 2019 through to (triangle) 2 October 2020 is  
120 plotted by the red line. Gray solid and dashed lines denote the approximate sea ice edge at the minimum (15  
121 September 2020) and the maximum (5 March 2020), respectively.

## 122 123 2.2 Meteorological and turbulence measurements near the surface

124 Meteorological and turbulence measurements were made from a tower on the sea ice at “Met City”,  
125 which was located 300–600 m away from the vessel (Cox et al., 2023). The u-Sonic-3 Cage MP anemometers  
126 by METEK GmbH and HMT300 air temperature sensors by Vaisala were fixed at nominal heights of 2 m, 6  
127 m, and 10 m on the meteorological tower. The tower was set up during the periods when the vessel passively  
128 drifted with an ice floe (i.e., from mid-October 2019 to mid-May 2020, from mid-June through July 2020,  
129 and from late August to mid-September 2020). The sampling frequency of fast response instruments (i.e., u-  
130 Sonic-3 Cage MP anemometer) was at 20 Hz, resampled to 10 Hz. To derive turbulence parameters, the  
131 following processes were carried out: despiking, block averaging over a 10-min interval, coordinate rotating  
132 via double rotation, frequency correcting, and virtual temperature correcting. In this study, sensible heat flux  
133 ( $SH$ , defined as positive upwards), near-surface air temperature at 2 m, friction velocity, and turbulent kinetic  
134 energy (TKE) dissipation rate are used. Based on a footprint analysis using the Kljun et al. (2015) model,  
135 90% of the sensible heat flux measurements have a source area fetch of no more than 275 m, a region that  
136 was typically dominated by consistent sea ice throughout the year. Although the sounding site may typically  
137 be outside the source region of these flux measurements, we assume the conditions at the two sites are  
138 equivalent, which is also assumed in the merged sounding-tower product.

139

## 2.3 Cloud properties derived from combined sensors

Cloud-related measurements come from ShupeTurner cloud microphysics product (Shupe, 2022). This product uses multiple measurement sources (e.g., cloud radar, ceilometer, depolarization lidar, and microwave radiometer) to derive time-height data, including cloud phase type and condensed water content for both liquid and ice. Details of the retrieval algorithm, its application, and uncertainties are provided in Shupe et al. (2015). In our study, the condensed water content data are linearly interpolated onto the vertical grid with resolution of 10 m for consistency. The cloud phase type data are used to determine clear and cloudy environments. A grid point is labeled as “cloudy” if clouds are identified in the upper and lower cloud phase type data points adjacent to the grid, otherwise it is labeled as “clear”.

## 3 ABLH determination method and algorithm evaluation

The most objective method of ABLH determination is based on profiles of turbulence measurements deployed on aircraft or other platforms, but such measurements were not routinely carried out during the MOSAiC expedition. Thus, the ABLH determination in our study is based on the thermal and dynamic structure of radiosoundings. In previous literature, the ABLH is determined through multiple profiles of atmospheric variables and manual visual inspection, which can be considered as the “observed” ABLH (Liu and Liang, 2010; Zhang et al., 2014; Jozef et al., 2022). In this section, we will describe the manually-labeled ABLH determination method and derive an ABLH for each sounding. Next, we will use these ABLHs as a reference to evaluate the automated ABLH algorithms provided by the PBLHT VAP. Finally, we will develop and evaluate an improved ABLH automated algorithm that is suitable for the Arctic atmosphere, and further discuss an important parameter for the algorithms and its stability dependence.

### 3.1 ABL regime classification and ABLH determination

The ABLH determination method starts with the classification of ABL regimes. Based on previous studies (e.g., Vogelezang and Holtslag, 1996; Liu and Liang, 2010), we divide the ABLs into three types: stable boundary layer (SBL), near-neutral boundary layer (NBL), and convective boundary layer (CBL), corresponding with three different stability states near the surface. We first use  $SH$  to diagnose the ABL regime types. The specific classification formula is presented below:

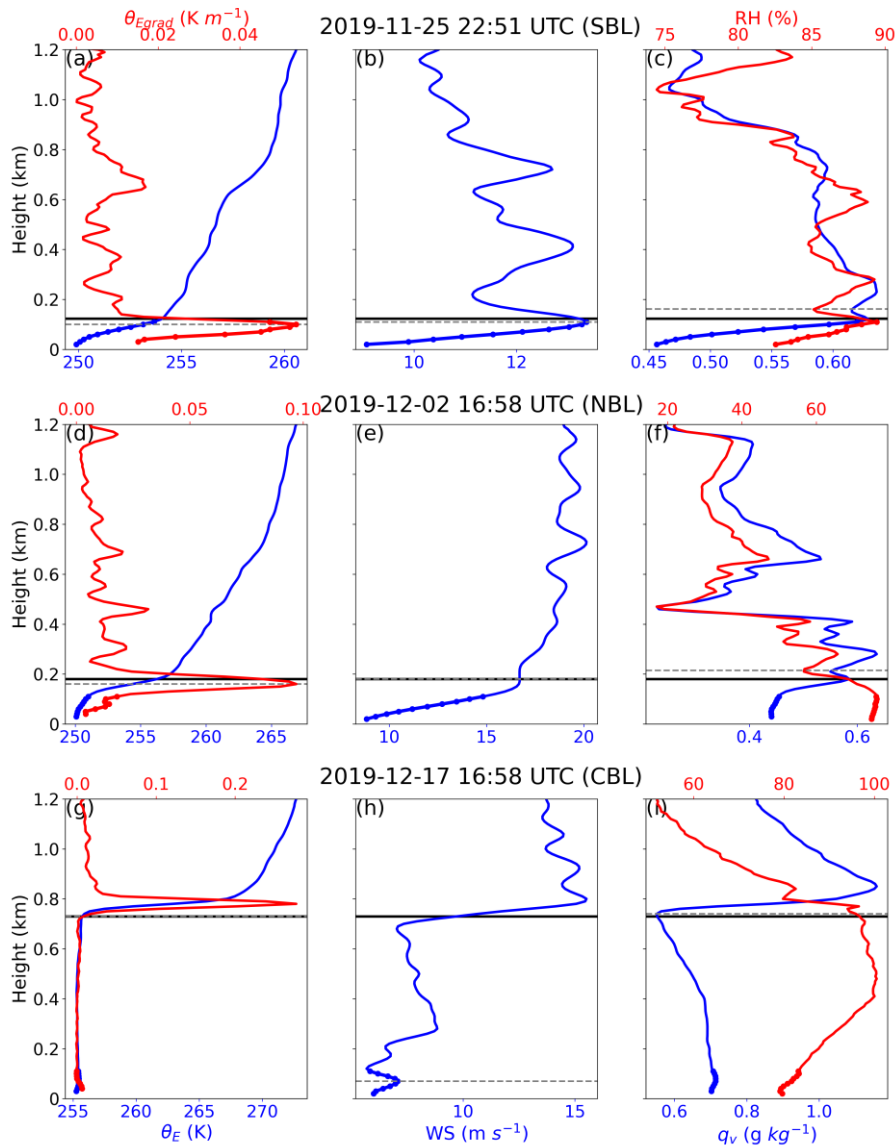
$$\begin{cases} SH > +\delta & \text{for CBL} \\ SH < -\delta & \text{for SBL, (1)} \\ \text{else} & \text{for NBL} \end{cases}$$

where  $\delta$  is the critical value that is specified as  $2 \text{ W m}^{-2}$ , following Steeneveld et al. (2007b). If corresponding  $SH$  data are unavailable, the difference of equivalent potential temperature ( $\theta_E$ ) between the 100 and 50 m heights ( $\theta_E$  difference) derived from the sounding profile is used to determine the ABL type. Specifically, if  $\theta_E$  difference is larger than 0.2 K, the ABL is identified as SBL; if  $\theta_E$  difference is less than -0.2 K, the ABL is identified as CBL; and other profiles are labeled as NBLs, roughly following Liu and Liang (2010).

The manually-labeled ABLH determination in our study is based on characteristics of sounding profiles and regime types. For each atmospheric sounding profile, equivalent potential temperature ( $\theta_E$ ), equivalent potential temperature gradient ( $\theta_{Egrad}$ ), wind speed ( $WS$ ), specific humidity ( $q_v$ ), and  $RH$  are used to obtain

177 multiple estimates of the ABLH, which are used to determine the final estimate. Three cases to describe the  
178 method are presented in Fig. 2. Figures 2 (a–c) are the case of a SBL, which features surface-based  
179 temperature and humidity inversions. Figures 2 (d–f) are the case of a NBL, with approximately constant  $\theta_E$   
180 from the surface up to the inversion base and strong horizontal wind. Figures 2 (g–i) are the case of a CBL,  
181 with a deeper well-mixed layer and low-level cloud coupled to the surface (e.g., Shupe et al., 2013). In terms  
182 of  $\theta_E$  profiles, the estimated ABLH is the level at which the  $\theta_{Egrad}$  reaches its maximum for SBL and NBL  
183 cases, and the base of the  $\theta_E$  inversion for CBL cases (Martucci et al., 2007). In terms of  $WS$  profiles, the  
184 ABLH is estimated to be the height of the  $WS$  maximum for all three regime types (Mahrt et al., 1979). In  
185 terms of humidity profiles, the estimated ABLH is the level at which the  $RH$  rapidly decreases for SBL and  
186 NBL cases, and the base of the  $q_v$  inversion for CBL cases (Lenschow et al., 2000). The manually-observed  
187 ABLHs (solid black lines in Fig. 2) are then determined through consideration of these three distinct  
188 estimates using the following rules: (1) If the estimates differ slightly from each other, take the average of  
189 these estimates as ABLH; (2) If a strong characteristic (sharp gradients or peaks) of the profile is evident,  
190 select the estimate obtained based on this characteristic; (3) If the ABL structure is similar to that at the  
191 previous time, select the estimate with the smallest change to ensure that ABLHs are consistent in time. It is  
192 evident that the lowest layers of profiles have a great impact on the ABLH determination, particularly for  
193 shallow SBLs and NBLs. Thus, the merged radiosonde-tower profiles help make the ABLH determination  
194 more reliable than when using radiosondes alone.

195



196  
197

198  
199  
200  
201  
202  
203  
204

205  
206

### 3.2 Automated algorithm evaluation

207  
208  
209  
210

Figure 2 Vertical profiles of (left) equivalent potential temperature ( $\theta_E$ ),  $\theta_E$  gradients ( $\theta_{Egrad}$ ), (middle) wind speed ( $WS$ ), and (right) relative humidity ( $RH$ ) and specific humidity ( $q_v$ ) at (a–c) 25 November 2019, 22:51 UTC, (d–f) 2 December 2019, 16:58 UTC, and (g–i) 17 December 2019 16:58 UTC. Boundary layers at the three times represent stable boundary layer (SBL), near-neutral boundary layer (NBL), and convective boundary layer (CBL), respectively. The gray dashed horizontal lines denote the atmospheric boundary-layer height (ABLH) estimates based only on the profile shown in that panel, and the black solid horizontal lines denote the manually observed ABLHs. The dots in the lowest 100 m denote the section of the profiles impacted by the radiosonde-tower merging.

The automated ABLH algorithms consist of various empirical formulas. Based on these empirical formulas, estimated ABLHs are determined automatically and without manual intervention. Therefore, these algorithms can perform real-time and fast calculations on large amounts of data and are widely used in model simulations (Seibert et al., 2000; Konor et al., 2009). However, automated algorithms might lead to large

211 errors in estimating ABLHs, and the parameter selection in these algorithms will have a great impact on the  
 212 results. In our study, estimated ABLHs obtained using three automated algorithms are compared with  
 213 manually-labeled ABLHs to evaluate their performance over the Arctic Ocean. These algorithms, including  
 214 the Liu-Liang algorithm, the Heffter algorithm, and the bulk Richardson number algorithm, are all available  
 215 in the PBLH VAP as described in Sivaraman et al. (2013). Here we give a brief description of the three  
 216 algorithms.

217 The Liu-Liang algorithm determines ABLH based on potential temperature and wind speed according to  
 218 Liu and Liang (2010). For CBL regimes, the definition of ABLH is the height at “which an air parcel rising  
 219 adiabatically from the surface becomes neutrally buoyant”, and the temperature excess value is 0.1 K. For  
 220 SBL regimes, two different estimates of the ABLH are obtained, if possible, based on stability criteria and  
 221 wind shear criteria, respectively. For stability, the ABLH is defined as the lowest level,  $k$ , at which the  $\theta_{Egrad}$   
 222 reaches a minimum and meets either of the following two conditions:

$$223 \quad \begin{cases} \theta_{Egrad\ k} - \theta_{Egrad\ k-1} < -40 \text{ K km}^{-1} \\ \theta_{Egrad\ k+1} < 0.5 \text{ K km}^{-1}, \theta_{Egrad\ k+2} < 0.5 \text{ K km}^{-1} \end{cases}, (2)$$

224 where the subscripts ( $k, k-1, k+1$ , and  $k+2$ ) represent the  $\theta_{Egrad}$  at corresponding levels. For wind shear, the  
 225 ABLH is defined as the height where the wind speed reaches a maximum that is at least  $2 \text{ m s}^{-1}$  stronger than  
 226 the layers immediately above and below while decreasing monotonically toward the surface (i.e., a low-level  
 227 jet). The final ABLH is defined as the lower of the two heights.

228 The Heffter algorithm, which was suggested by Heffter (1980), is a widely used algorithm (e.g., Marsik  
 229 et al., 1995; Snyder and Strawbridge, 2004). The algorithm determines ABLH through the strength of the  
 230 inversion and potential temperature difference across the inversion. The ABLH is defined as the lowest layer  
 231 in which the potential temperature difference between the top and bottom of the inversion is greater than 2  
 232 K. If no layer meets the criteria, the ABLH is defined as the layer at which the potential temperature gradient  
 233 reaches the largest maximum.

234 The bulk Richardson number algorithm is based on the profile of the bulk Richardson number ( $Ri_b$ ), and  
 235 has been shown to be a reliable algorithm for determining ABLHs (Seidel et al., 2012).  $Ri_b$  is a dimensionless  
 236 number that represents the ratio of thermally produced turbulence to that induced by mechanical shear. The  
 237  $Ri_b$  formula used in the PBLH VAP (Sørensen et al., 1998; Sivaraman et al., 2013) is expressed as:

$$238 \quad Ri_b = \left( \frac{gh}{\theta_{v0}} \right) \left( \frac{\theta_{vh} - \theta_{v0}}{u_h^2 + v_h^2} \right), (3)$$

239 where  $g$  is the acceleration of gravity;  $\theta_{vh}$  and  $\theta_{v0}$  are the virtual potential temperature at height  $h$  and the  
 240 surface, respectively;  $u_h$  and  $v_h$  are the horizontal wind speed component at height  $h$ . The ABLH is defined  
 241 as the height of  $Ri_b$  exceeding a critical threshold (the critical bulk Richardson number,  $Ri_{bc}$ ; Seibert et al.,  
 242 2000). The PBLH VAP includes ABLH estimates based on two widely used  $Ri_{bc}$  values: 0.25 and 0.5.

243 To quantitatively evaluate the performance of each automatic algorithm, we introduce the correlation  
 244 coefficient  $R$  and two other statistical measures: the dimensionless *Bias* and the median absolute error  
 245 (*MEAE*; Steeneveld et al., 2007a). The formulas are as follows:

$$246 \quad Bias = \frac{2}{n} \sum_{i=1}^n \frac{H_{auto} - H_{obs}}{H_{auto} + H_{obs}}, (4)$$



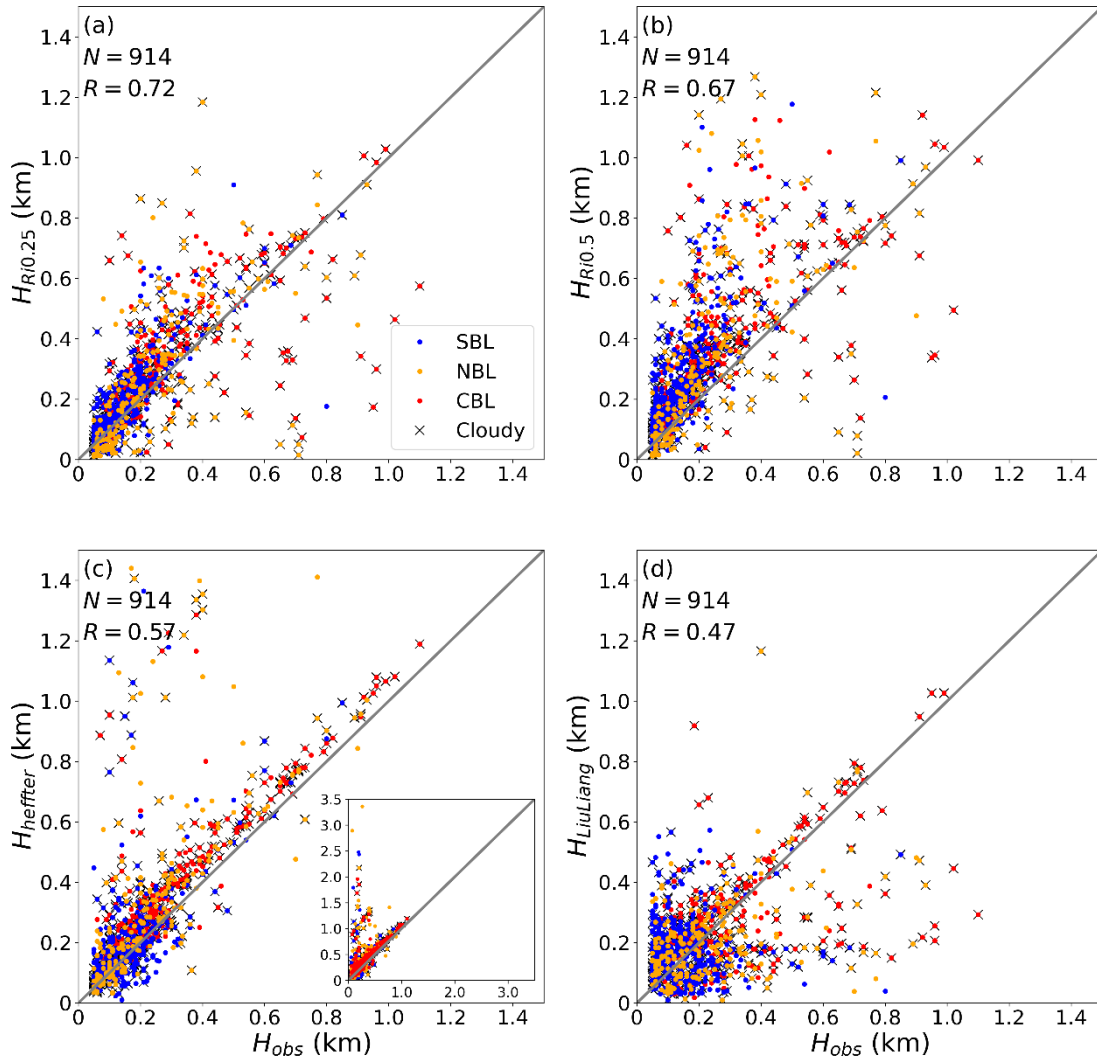
247 
$$MEAE = \text{median}(|H_{auto} - H_{obs}|), (5)$$

248 where  $H_{auto}$  is the ABLH obtained by the automated algorithm;  $H_{obs}$  is the ABLH manually determined;  $n$  is  
249 the number of valid sounding profile samples. According to the definitions of these statistical measures,  
250 larger  $R$  and smaller  $Bias$  and MEAE mean a better performance of the automated algorithm.

251 We also analyze the algorithm performances for cloudy and clear conditions, considering that low-level  
252 clouds containing liquid water play an important role in the Arctic ABL (Shupe and Intrieri, 2004; Brooks et  
253 al., 2017). In our study, the  $RH$  threshold of 96% (Silber and Shupe, 2022) and the cloud source flag data are  
254 used for cloud detection. If a cloud is detected in the cloud source flag data and the  $RH$  is larger than 96%,  
255 then the profile is labeled as cloudy. The sounding profiles that contain at least one identified cloud layer  
256 below 1500 m are classified as “cloudy”, and as “clear” otherwise.

257 Figure 3 presents the comparisons of estimated ABLHs with the manually-labeled ABLHs, and the  
258 associated statistical measures are given in Table 1. The results show that the  $Ri_b$  algorithm with  $Ri_{bc}$  of 0.25  
259 performs best overall, and particularly for SBL cases. The performance of the  $Ri_b$  algorithm with  $Ri_{bc}$  of 0.5  
260 is poorer than that of the  $Ri_b$  algorithm with  $Ri_{bc}$  of 0.25, with overestimations of ABLHs in general, and  
261 larger errors with lower correlation coefficients for all types of ABLs. The Heffter algorithm performs well  
262 in cases of high ABLH and particularly for cloudy and CBL cases, but does significantly overestimate ABLH  
263 in a large number of cases as shown in the Fig. 3c subgraph. This is attributed to the determination criterion  
264 of the Heffter algorithm, i.e., ABLHs are determined by inversion layers, which means that large errors occur  
265 when the inversion layer is higher than the mixed layer. Additionally, while the Heffter performance in many  
266 of the ABL conditions is only marginally worse statistically than the  $Ri_b$  algorithm with  $Ri_{bc}$  of 0.25, its  
267 correlations are notably worse for SBL and NBL cases. The performance of the Liu-Liang algorithm is  
268 generally poorer than the other algorithms, particularly for correlation coefficient, which is probably due to  
269 the impact of noise in the lower ABLH profiles and unsuitable parameters in the algorithm. In summary, the  
270  $Ri_b$  algorithm is reliable over the Arctic Ocean and performs better than other algorithms, and this result  
271 agrees with Jozef et al. (2022). Furthermore, we will explore ways to improve the  $Ri_b$  algorithm to make it  
272 more suitable for cloudy and convective conditions.

273



274  
 275 Figure 3 Comparisons of the ABLHs determined from radiosonde profiles using the bulk Richardson number  
 276 ( $Ri_b$ ) algorithm with the critical values ( $Ri_{bc}$ ) of (a) 0.25 and (b) 0.5, (c) the Heffter algorithm, and (d) the  
 277 Liu-Liang algorithm with the manually-identified "observed" ABLHs. The blue, yellow, and red colors  
 278 indicate regime types of SBL, NBL, and CBL, respectively. The "x" signs indicate the Cloudy ABLs. The  
 279 case numbers ( $N$ ) and correlation coefficients ( $R$ ) are given in each panel. The subgraph in (c) denotes all  
 280 data points ranging from 0 to 3.5 km.

281  
 282  
 283  
 284  
 285  
 286  
 287  
 288  
 289

290 Table 1 The statistical measures ( $R$ ,  $Bias$ ,  $MEAE$ ) for the four algorithms applied to the radiosonde dataset.  
 291 All correlation coefficients are statistically significant ( $p < 0.05$ ), except for SBL types in the Liu-Liang  
 292 algorithm.

Algorithm	Regime type	$R$	Bias	MEAE (m)
<b>The <math>Ri_b</math> algorithm with <math>Ri_{bc} = 0.25</math></b>	ALL	0.72	0.10	50
	SBL	0.81	0.16	34
	NBL	0.68	-0.04	62
	CBL	0.65	0.15	71
	Cloudy	0.69	0.08	51
<b>The <math>Ri_b</math> algorithm with <math>Ri_{bc} = 0.5</math></b>	ALL	0.67	0.40	97
	SBL	0.73	0.50	88
	NBL	0.61	0.23	91
	CBL	0.60	0.39	120
	Cloudy	0.66	0.36	94
<b>The Heffter algorithm</b>	ALL	0.57	0.23	53
	SBL	0.46	0.17	33
	NBL	0.45	0.30	59
	CBL	0.66	0.28	74
	Cloudy	0.68	0.25	59
<b>The Liu-Liang algorithm</b>	ALL	0.47	0.04	82
	SBL	0.05	0.15	90
	NBL	0.44	-0.07	81
	CBL	0.56	-0.05	69
	Cloudy	0.52	-0.01	82
<b>The improved <math>Ri</math> algorithm with <math>Ri_{bc} = 0.35</math></b>	ALL	0.85	-0.06	29
	SBL	0.79	-0.08	21
	NBL	0.79	-0.18	35
	CBL	0.87	0.05	36
	Cloudy	0.86	-0.03	30

293  
294

### 295 3.3 An improved $Ri$ algorithm considering the cloud effect

296 As a traditional  $Ri_b$  formula, Eq. (3) may break down in cases of ABLs with relatively high wind speed  
 297 and upper-level stratification due to the overestimation of shear production (Kim and Mahrt, 1992).  
 298 Vogelezang and Holtslag (1996) proposed a finite-difference  $Ri$  formula, which is expressed as:

$$299 Ri_F = \frac{(g/\theta_{vs})(\theta_{vh}-\theta_{vs})(h-z_s)}{(u_h-u_s)^2+(v_h-v_s)^2+bu_*^2}, \quad (6)$$

300 where  $z_s$  is the lower boundary for the ABL,  $\theta_{vs}$ ,  $u_s$ , and  $v_s$  are the  $\theta_v$  and wind components at the height  $z_s$ ,  
 301 respectively,  $b$  is an empirical coefficient, and  $u_*$  is the surface friction velocity.  $Ri_F$  is considered for a parcel  
 302 located somewhat above the surface to avoid the above problem, and  $u_*$  is also taken into account to avoid  
 303 underestimation in the situation of a uniform wind profile in the upper layer. Here, we use  $Ri_F$  for clear-sky  
 304 profiles and take  $z_s$  and  $b$  values as 40 m and 100, respectively, according to Zhang et al. (2020).

305 As shown in Fig. 3, the estimations of cloudy ABLHs are sometimes quite poor, which motivates us to further  
 306 improve the algorithm. Under cloudy conditions, the moist Richardson number ( $Ri_m$ ) can be used to include  
 307 cloud effects on the buoyancy term. Brooks et al. (2017) adopted the  $Ri_m$  formula expressed as:

$$308 Ri_m = \frac{\left(\frac{g}{T}\right)\left(\frac{dT}{dz} + \Gamma_m\right)\left(1 + \frac{Lq_s}{RT}\right) - \frac{g}{1+q_w} \frac{dq_w}{dz}}{\left(\frac{du}{dz}\right)^2 + \left(\frac{dv}{dz}\right)^2}, \quad (7)$$

309 where  $T$  is air temperature,  $\Gamma_m$  is the moist adiabatic lapse rate,  $L$  is the latent heat of vaporization,  $q_s$  is the

310 saturation mixing ratio, and  $q_w$  is the total water mixing ratio, i.e.,  $q_w = q_s + q_L$ , where  $q_L$  is the liquid water  
 311 mixing ratio and is obtained based on the condensed water content. However, Eq. (6) is a gradient  $Ri$  and is  
 312 calculated based on local gradients of wind speed, temperature, and humidity. To be consistent with the  $Ri$   
 313 formula proposed by Vogelezang and Holtslag (1996), we rewrite the formula in a finite-difference form  
 314 expressed as:

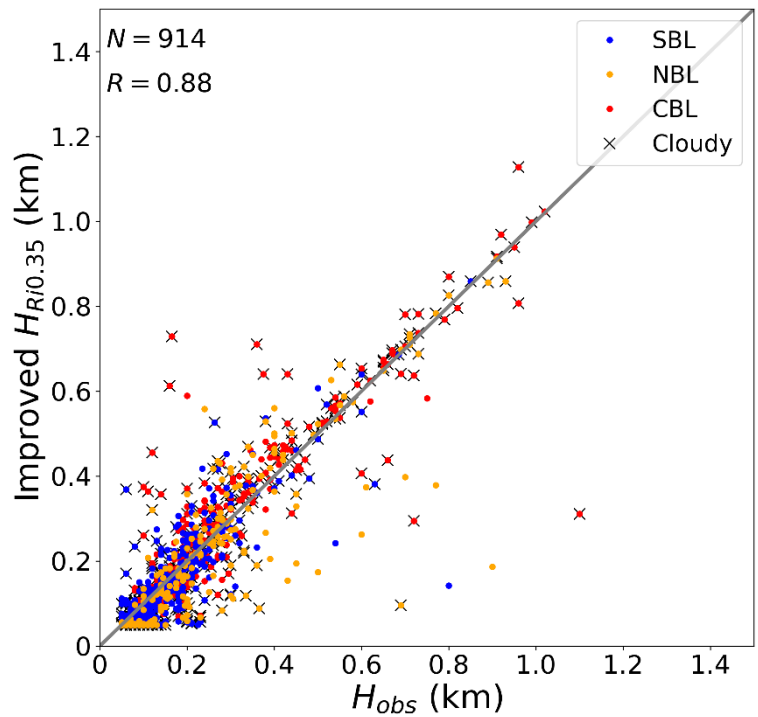
$$315 \quad Ri_m = \frac{\left[ (g/T_s) \left( \frac{T_h - T_s}{h - z_s} + \Gamma_m \right) \left( 1 + \frac{Lq_{sh}}{RT_h} \right) - \frac{g}{1 + q_{wh}} \frac{q_{wh} - q_{ws}}{h - z_s} \right] (h - z_s)^2}{(u_h - u_s)^2 + (v_h - v_s)^2 + bu_*^2}, \quad (8)$$

316 where subscripts ( $h$  and  $s$ ) of the variables denote the calculated height, similar to Eq. (6), but note that the  
 317  $s$  and  $z_s$  are adjusted to 130 m, given the cloud radar blind zone. Considering that  $Ri_m$  is only appropriate for  
 318 the liquid-bearing cloud cases, we use the  $Ri_F$  for “clear” grid points and use  $Ri_m$  for “cloudy” grid cells.  
 319 Using this improved approach, we evaluated the best value of  $Ri_c$  to minimize the errors compared to the  
 320 reference data set, arriving at an optimal value of  $Ri_c = 0.35$ . The comparison of ABLH estimates obtained  
 321 through the improved  $Ri$  algorithm with the manually-labeled ABLHs demonstrates significant improvement  
 322 relative to other algorithms, particularly for cloudy conditions (Fig. 4, Table 1).

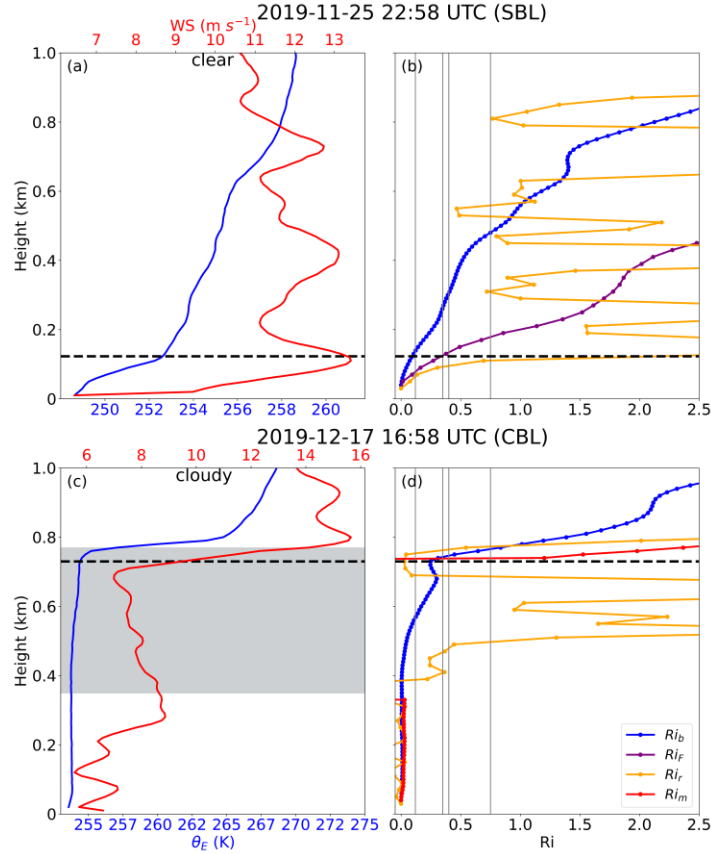
323 Since some other studies have proposed different  $Ri_c$  values for MOSAiC (e.g., Jozef et al., 2022; Barten  
 324 et al., 2023; Akansu et al., 2023), we will discuss the difference in  $Ri_c$  values here. The first thing to make  
 325 clear is that these studies use different formulas to obtain  $Ri$  profiles. Barten et al. (2023) and Akansu et al.  
 326 (2023) both use the traditional  $Ri_b$  algorithm based on Eq. (3), while they used  $Ri_c$  values of 0.4 and 0.12,  
 327 respectively. This difference was likely caused by the different methods to manually derive their reference  
 328 ABLH data sets. Jozef et al. (2022) calculates the  $Ri$  over a rolling 30 m altitude range, labeled as  $Ri_r$ , and  
 329 the criterion is modified to require four consecutive data points to be above the  $Ri_c$  of 0.75. In our study, we  
 330 use  $Ri_F$  proposed by Vogelezang and Holtslag (1996) for clear-sky conditions, and  $Ri_m$  for cloudy conditions.  
 331 Based on the results presented here, it is apparent that this more complex approach improves the error  
 332 statistics relative to approaches based on Eq. (3). In addition, some of the differences may also related to  
 333 authors using different data sets or time periods. For instance, Akansu et al. (2023) primarily used sounding  
 334 data based on tether balloon for a specific sub-period of MOSAiC, and Jozef et al. (2022) used radiosondes  
 335 from when they had concurrent UAV observations. The data used in our study are based on merged sounding-  
 336 tower product, as mentioned above.

337 To further explore the differences among the four different approaches, we examine one SBL and CBL  
 338 case. For a clear-sky SBL case (Fig. 5 a, b), the approaches from Akansu et al., Jozef et al. (2022), and this  
 339 study all agree closely with the manual ABLH, while the Barten et al. approach results in a significant  
 340 overestimation. For a cloudy-sky CBL case (Fig. 5 c, d), the approach from this study agrees with the manual  
 341 ABLH, while the approach from Barten et al. overestimates the ABLH by about 30 m, and the approaches  
 342 from Akansu et al. and Jozef et al. (2022) underestimate the ABLH by 130 m and 230 m, respectively. These  
 343 results further demonstrate how  $Ri_c$  depends on the choice of  $Ri$  formula. Moreover,  $Ri_c$  is not analytically  
 344 derived from basic physical principles (Zilitinkevich et al. 2007), and the concept of  $Ri_c$  is challenged by  
 345 non-steady regimes (Zilitinkevich and Baklanov, 2002) and the hysteresis phenomenon (Banta et al., 2003;

346 Tjernström et al., 2009). Therefore, an objective  $Ri_c$  does not exist. Rather, it is empirically used as an  
347 algorithmic parameter to simply derive the ABLH.  
348



349  
350 Figure 4 Similar to Fig. 3, but for the comparison of the ABLHs determined by the improved  $Ri$  algorithm  
351 with the observed ABLHs. The case number ( $N$ ) and correlation coefficient ( $R$ ) are given.  
352



353

354 Figure 5 Vertical profiles of (left)  $\theta_E$  and wind speed, and (right)  $Ri$  based on different formulas at (a–b) 25  
 355 November 2019, 22:58 UTC and (c–d) 17 December 2019, 16:58 UTC. Boundary layers at the two times  
 356 represent a clear-sky SBL and a cloudy-sky CBL respectively. The black dashed horizontal lines denote the  
 357 manually-identified ABLH, and the gray solid vertical lines denote the different  $Ri_c$  values, including 0.12,  
 358 0.35, 0.4, and 0.75. The gray shading in (c) denotes the cloud layer.

359

### 360 3.4 The stability dependence of critical Richardson number

361 Richardson et al. (2013) and Basu et al. (2014) suggested that there is a stability dependence of  $Ri_c$  in  
 362 stable conditions, which is different from the constant  $Ri_c = 0.35$  used in our improved algorithm. In this  
 363 section, we will discuss the impact of this dependence on ABLH estimation. We use the improved  $Ri$   
 364 algorithm to calculate the  $Ri$  at the manually-labeled ABLH ( $h$ ). This new parameter is named  $Ri_h$  to  
 365 distinguish it from the constant  $Ri_c$ . To be consistent with Basu et al. (2014), the bulk stability parameter  $h/L$   
 366 is used for our analysis, where  $L$  is the Obukhov length at the surface. Based on these two variables, the  
 367 stability dependence can be expressed as:

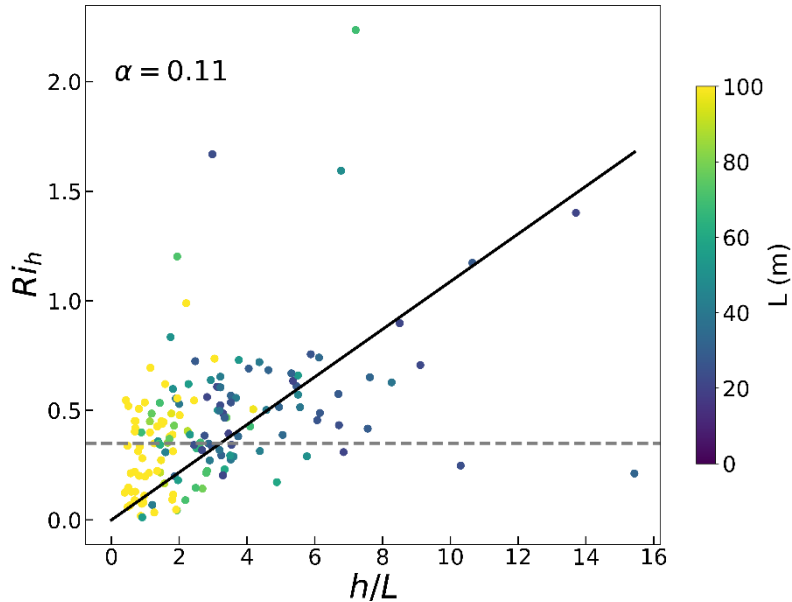
$$368 Ri_h = \alpha \frac{h}{L}, \quad (9)$$

369 where  $\alpha$  is a proportionality constant. As suggested in Basu et al. (2014), the data for convective, near-neutral,  
 370 and very stable conditions are excluded to obtain a credible  $\alpha$ . Specifically, data points that meet the  
 371 thresholds ( $L > 500$  m and  $L < L_{min}$ ) are excluded in our analysis, where the  $L_{min}$  corresponds to the heat flux  
 372 minimum (Basu et al. 2008) and is assumed as 20 m here. Finally, we select 168 samples. The  $Ri_h$  plotted as

373 a function of  $h/L$  for these selected data is presented in Fig. 6, and the value of  $L$  is colored to probe if the  
 374 dependence is simply due to self-correlation. The results show  $Ri_h$  values that mostly range from 0 to 0.75,  
 375 and the best-fit line indicates an overall positive correlation trend, with  $\alpha = 0.11$ . The  $\alpha$  value is somewhat  
 376 larger than the results in Richardson et al. (2013) and Basu et al. (2014), which is attributed to the different  
 377  $Ri$  algorithm used in our study. In addition, if a few of the extreme points are removed, the bulk of the data  
 378 does not show a strong  $h/L$  dependence and is instead fairly well represented by a constant  $Ri_h = 0.35$ , which  
 379 is also suitable for convective conditions (e.g., Fig. 5c, d).

380 In summary, we assess the stability dependence of  $Ri_c$  based on our improved  $Ri$  algorithm, and the  
 381 results present an overall positive correlation trend. However, this type of stability dependence of  $Ri_c$  is  
 382 challenged to be used in practical applications because the sensitivity of  $\alpha$  to surface characteristics and  
 383 atmospheric conditions can additionally degrade the accuracy of ABLH estimates. In addition, Eq. (9)  
 384 requires a priori determination of the ABLH, which also causes difficulties for practical applications of such  
 385 an approach. Therefore, we still use the  $Ri$  algorithm with fixed  $Ri_c = 0.35$  for simplicity.

386



387

388 Figure 6  $Ri_h$  versus  $h/L$  for selected cases. The data points are colored based on the value of  $L$ . The black  
 389 solid line is the best fit for the selected data points, and the best-fit  $\alpha$  value is also given. The gray dashed  
 390 line is the constant  $Ri_c = 0.35$  used in the improved  $Ri$  algorithm.

391

392

## 393 4 MOSAiC ABLH variation and controlling factors

### 394 4.1 Overall distribution of ABLH

395 In this section, we analyze the ABLH variation during the MOSAiC and relevant controlling factors,  
 396 based on the manually-labeled ABLH dataset and the ABL types that are determined through Eq. (1), or only  
 397 the  $\theta_E$  difference if SH is unavailable. The full-time series of ABLH during the MOSAiC expedition is  
 398 presented in Fig. 7 and forms the basis for the remaining analyses. According to near surface conditions and

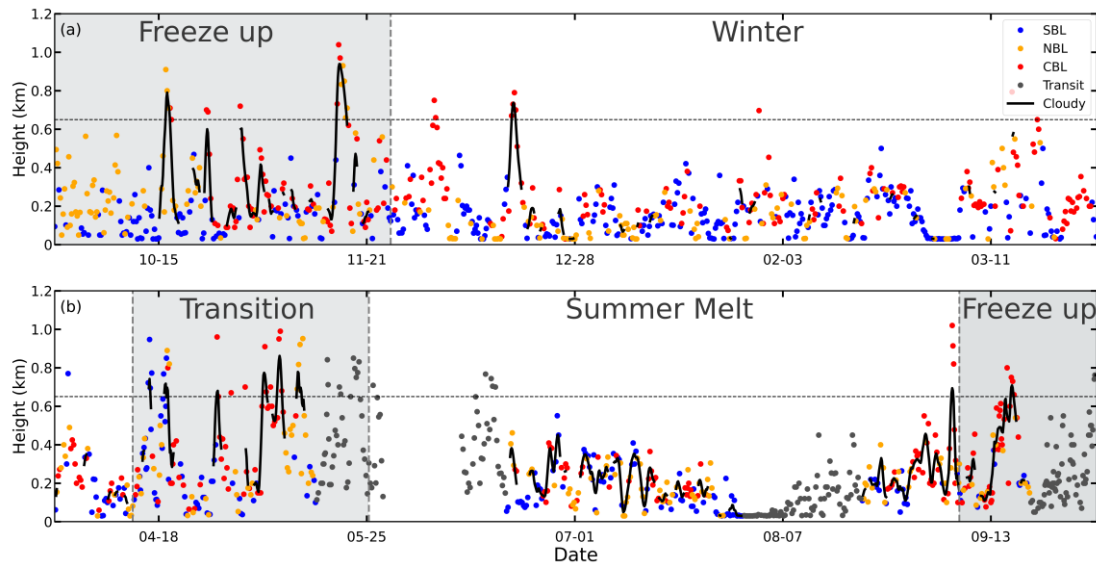
399 the sea ice state, the whole MOSAiC observation period is divided into “freeze up”, “winter”, “transition”,  
400 and “summer melt” periods (Shupe et al., 2022), roughly corresponding to the seasons of autumn, winter,  
401 spring, and summer, respectively. In Figure 7, the black solid lines indicate persistent low-level clouds that  
402 exist for more than 12 h; these occur most frequently in the late summer and autumn (the “freeze up” period),  
403 which agrees with Shupe et al. (2011). Note that the grey dots indicate that the ABL data were observed  
404 while the vessel was in transit, and the representativity of the ABLH data should be considered in this context.  
405 For the first such period, the vessel left the MOSAiC ice floe in mid-May and slowly progressed south  
406 through tightly consolidated sea ice, such that the data are generally representative of the sea ice pack in the  
407 region. Measurements from early June when the vessel was near or in open water close to Svalbard have  
408 been excluded entirely from the analysis. In the middle of June, as the vessel returned to the original  
409 MOSAiC ice floe, the sea ice was not as tightly consolidated and the vessel preferentially went through leads;  
410 the preferentially lower ice fraction along this transit could have impacted the thermal structure of the ABL.  
411 For the three weeks in early August, the vessel moved around in the Fram Strait area and then made its way  
412 north to another passive sea ice drifting position near the North Pole, again transiting through regions with  
413 lower sea ice fraction. Finally, at the very end of the expedition, the vessel took some time to exit the sea ice,  
414 stopping a few times to allow for work on the ice.

415 Overall, as shown in Fig. 7, the mean ABLH during the whole observation period is 231 m. This is  
416 lower than the typical ABLH over the Arctic land surface (Liu and Liang, 2010), which is primarily attributed  
417 to the stronger suppression of the temperature inversion over the sea-ice surface. The Arctic ABL is  
418 suppressed for most of the MOSAiC year, while for a few periods it intensively develops for several days at  
419 a time, most commonly when clouds and a CBL are present. For instance, frequent, intensive ABL  
420 development occurs in the “transition” period from 13 April through to 24 May 2020. In this period, the  
421 convective thermal structure and cloud effects contribute to ABLH reaching over the 95th percentile of the  
422 ABLH data (horizontal dotted line) for about 7 days, with the maximum ABLH of 1100 m. In contrast, the  
423 ABL is strongly suppressed in the period from 15 July through to 30 August 2020, with a mean ABLH of  
424 only 136 m. The specific mechanisms of ABL development and suppression in these two cases will be  
425 analyzed in Sections 4.3 and 4.4, respectively.

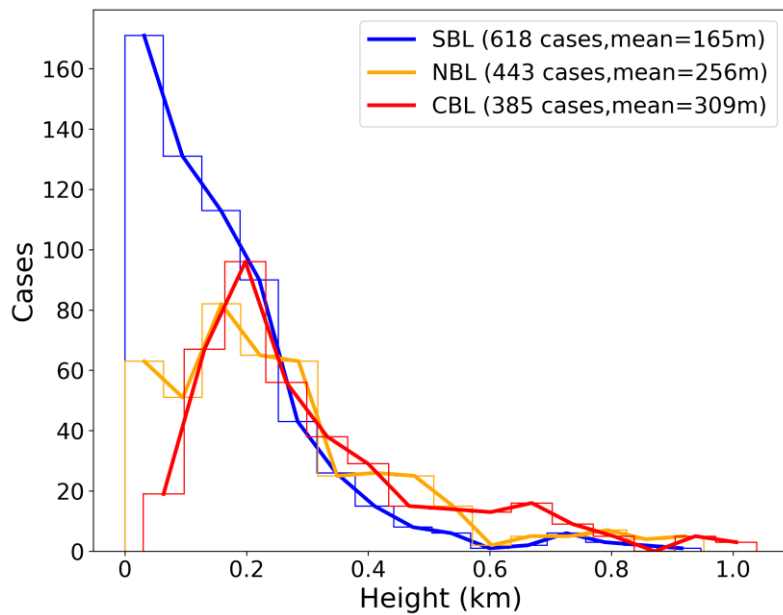
426 Figure 8 presents the frequency distribution of ABLH under SBL, NBL, and CBL regime types. Overall,  
427 the sample number of SBL cases is more than that of NBL and CBL cases during the MOSAiC period (43 %  
428 for SBL, 31% for NBL, and 26 % for CBL). These occurrence frequencies roughly agree with Jozef et al.  
429 (2023), while their results show more NBL and CBL and less SBL. It is likely to be attributed to differences  
430 in classification criteria. The distributions of SBL and NBL ABLH are skewed towards small values, with  
431 94 % and 79% of the ABLH values lower than 400 m, and mean values of 165 m and 256 m, respectively.  
432 For CBL, the distribution is shifted somewhat towards larger values, with 23 % of the ABLH values higher  
433 than 600 m and a mean value of 309 m.

434





435  
 436 Figure 7 Time series of ABLHs throughout the MOSAiC year is divided into (a) and (b). The blue, yellow,  
 437 and red dots indicate the heights of SBL, NBL, and CBL, respectively. The gray dots indicate ABL data  
 438 observed while the vessel was in transit. The black solid lines indicate the heights of cloudy ABLs and persist  
 439 for at least 12 hours. The gray dashed horizontal line denotes the 95th percentile of ABLH (650 m). The gray  
 440 and white background shadings indicate the periods under different surface-melting states, i.e., “freeze up”,  
 441 “winter”, “transition”, and “summer melt” periods.  
 442



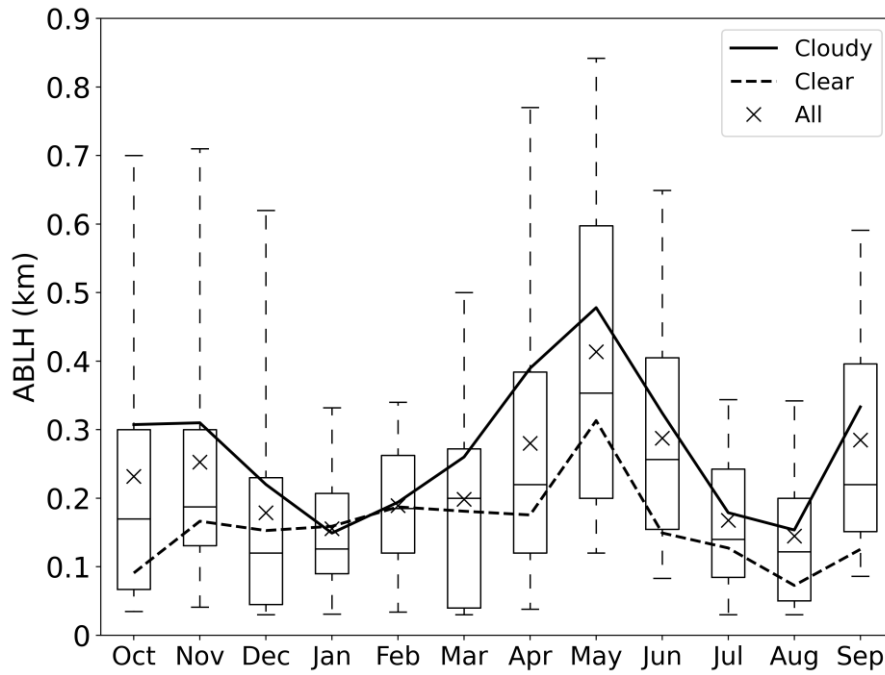
443  
 444 Figure 8 Frequency distribution of SBL height (blue), NBL height (yellow), and CBL height (red). The case  
 445 numbers and the mean values of ABLH for SBL, NBL, and CBL conditions are also given.  
 446

#### 447 4.2 Annual cycle of ABLH and related factors

448 Figure 9 presents the annual cycle of monthly ABLH statistics during the MOSAiC expedition in terms  
 449 of 5th, 25th, 50th, 75th, and 95th percentiles of ABLH (boxplots) and the mean value (“x” signs and solid

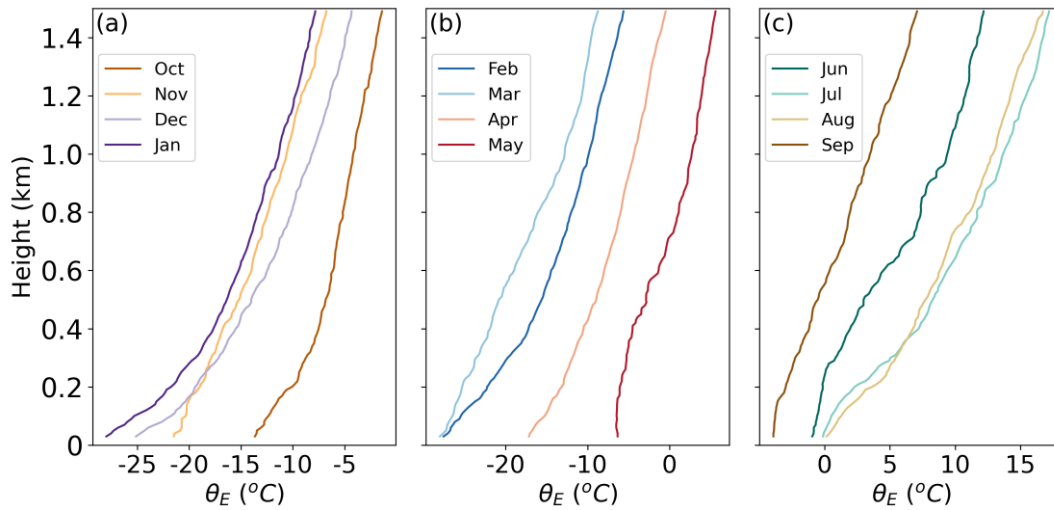
450 and dashed lines). The box-and-whisker plots show a distinct peak in May, with a median value of 363 m  
451 and the 95th percentile reaching over 800 m. An abrupt decrease occurs in the following July and August,  
452 and another minimum occurs in January, all with median values below 150 m. It should be noted that the  
453 ABLH data in transit (gray dots in Fig. 7) are also included in the statistics, which could have [been potentially](#)  
454 [impacted by more open-surface water conditions](#). Specifically, the ABLH data during transit periods cause  
455 higher mean ABLH for June and lower mean ABLH for August (see Fig. 7). The comparison between cloudy  
456 and clear-sky ABLHs indicates that the low-level clouds significantly contribute to the Arctic ABL  
457 development during the MOSAiC year, except in winter, when low-level clouds are rare.

458 The annual cycle of ABLH is determined by the seasonal evolution of the ABL structure (Tjernström  
459 et al., 2009; Palo et al., 2017), as revealed through median profiles of  $\theta_E$  in each month (Fig. 10). The results  
460 show that from the start of the MOSAiC expedition (October 2019), the near-surface  $\theta_E$  gradually decreases  
461 due to seasonal surface radiative cooling in the absence of sunlight, more rapidly than the atmosphere cools,  
462 which causes a strong surface temperature inversion. The increasing inversion strength through January leads  
463 to decreasing ABLH into “winter.” In February and March, the surface remains steady while the atmosphere  
464 cools more, leading to diminished temperature inversion strength and a small increase in ABLH. After March  
465 2020, with the return of sunlight, the  $\theta_E$  starts to rise over the whole lower atmosphere, and the near-surface  
466 air temperature warms somewhat more than the atmosphere above. This differential warming leads to more  
467 frequent near-neutral or convective thermal structures and contributes to high ABLH during the “transition”  
468 period. In July and August, the upper-layer temperature continues to rise while the near-surface temperature  
469 is constrained to  $\sim 0$  °C due to the melting sea ice surface, which leads again to a surface inversion and a  
470 diminished ABLH during the “summer melt” period. In September, as the sun descends to much lower angles,  
471 the  $\theta_E$  across the whole lower atmosphere starts to drop, with more rapid cooling in the atmosphere relative  
472 to the near-surface resulting again in near-neutral or convective thermal structures and an increase in the  
473 CBL height during the “freeze up” period. The whole process forms these general shifts over the annual  
474 cycle. In addition, we examined the potential implications of the diurnal cycle on the ABL thermal structure.  
475 Monthly profiles based on different moments of a day were found to show little variability (not shown), such  
476 that the impact of the diurnal cycle is minimal.



477  
478  
479  
480  
481  
482

Figure 9 Box-and-whisker plots of the ABLH distribution in each month throughout the MOSAiC year. The whiskers, the boxes, and the black horizontal lines show the 5th, 25th, 50th, 75th, and 95th percentile values of ABLH. The solid and dashed lines and the “x” signs indicate the mean ABLH of cloudy, clear, and all ABL types, respectively.



483  
484  
485  
486

Figure 10 Monthly median profiles of equivalent potential temperature throughout the MOSAiC year. The panel (a) represents Oct-Jan, panel (b) Feb-May and panel (c) Jun-Sep.

487 To further explore the relations between surface conditions and the ABLH, we evaluate the correlations  
488 between the ABLH and three near-surface meteorological and turbulence parameters during the MOSAiC  
489 period, including the near-surface equivalent potential temperature gradient ( $\theta_{Egrad} = \theta_{E 10m} - \theta_{E 2m}$ ), friction  
490 velocity ( $u_*$ ), and TKE dissipation rate ( $\epsilon$ ). The results are shown in Fig. 11. Generally, the near-surface  
491 buoyancy and shear effects both modulate these variables. In Fig. 11a, the ABLH distribution for negative

492  $\theta_{Egrad}$  has a wide range from the lowest level to above 1 km. As  $\theta_{Egrad}$  becomes positive and increases, the  
 493 ABLH distribution rapidly narrows to below 200 m. In general, positive  $\theta_{Egrad}$  means a stably stratified ABL  
 494 and surface-based temperature inversion, both of which lead to low ABLH, and negative  $\theta_{Egrad}$  means that  
 495 atmospheric stability near the surface is near-neutral or convective, which is necessary for ABL development.  
 496 The  $u_*$  presents a significant correlation with the ABLH, with correlation coefficient of 0.58 (Fig. 11b). High  
 497  $u_*$  values, which are related to strong mechanical mixing, contribute to the ABL development. However, it  
 498 is worth noting that intensive ABL development (ABLH over 600 m) only occurs as  $u_*$  ranges between 0.2  
 499 and 0.5 m s<sup>-1</sup>, which suggests that other factors exist to facilitate further development of the ABL, such as  
 500 cloud effects (see Fig. 9).  $\varepsilon$  indicates the rate at which the TKE is changing, and the high value of  $\varepsilon$   
 501 means well-developed turbulence. In Fig. 11c, when  $\varepsilon$  is less than  $5 \times 10^{-5}$  m<sup>2</sup> s<sup>-3</sup>, turbulence in the ABL is  
 502 limited with almost all ABLH values below 200 m. As  $\varepsilon$  increases and becomes larger than  $5 \times 10^{-5}$  m<sup>2</sup> s<sup>-3</sup>,  
 503 the average ABLH increases with active turbulent mixing in the ABL. The threshold of  $5 \times 10^{-5}$  m<sup>2</sup> s<sup>-3</sup> is  
 504 proposed by Brooks et al. (2017) as the distinction between turbulent and non-turbulent flows.

505 The free-flow stability (characterized by the free-flow Brunt-Väisälä frequency,  $N$ ) can affect the ABLH  
 506 (Zilitinkevich et al., 2002; Zilitinkevich and Baklanov, 2002; Zilitinkevich and Esau, 2002, 2003), and  
 507 therefore is also examined here. Based on the buoyancy flux at the surface ( $B_s$ ) and  $N$ , the NBLs and SBLs  
 508 can be further divided into four types: the truly neutral (TN,  $B_s = 0$  and  $N = 0$ ), the conventionally neutral  
 509 (CN,  $B_s = 0$  and  $N > 0$ ), the nocturnal stable (NS,  $B_s < 0$  and  $N = 0$ ), and the long-lived stable boundary layer  
 510 (LS,  $B_s < 0$  and  $N > 0$ ). According to Zilitinkevich and Baklanov (2002), we calculate the  $N$  and  $B_s$  and  
 511 reclassify the SBLs and NBLs. We find that the percentages of  $N > 0.015$  in SBLs and NBLs are 89 % and  
 512 80 %, which indicates that LS and CN types dominate the stable and neutral conditions for MOSAiC,  
 513 respectively. Since only 80 TN cases were identified, these are deemed to be too few for additional analysis  
 514 of this type. Zilitinkevich and Esau (2003) gave ABLH equations relevant to each ABL type as:

$$515 \quad h_E = \begin{cases} C_N u_* |fN|^{-1/2} & \text{(Pollard et al., 1973)} & \text{for CN ABL, (10)} \\ C_S u_*^2 |fB_s|^{-1/2} & \text{(Zilitinkevich, 1972)} & \text{for NS and LS ABL, (11)} \end{cases}$$

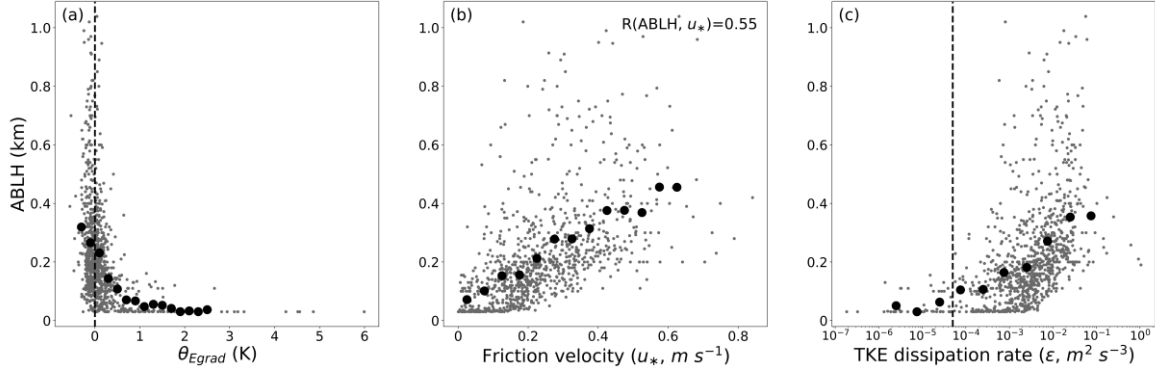
516 where  $h_E$  is the equilibrium ABLH,  $f$  is the Coriolis parameter, and  $C_N$  and  $C_S$  are empirical coefficients. In  
 517 addition, Vogelezang and Holtslag (1996) and Steeneveld et al. (2007a) also explore a  $h_E$  equation without  
 518 taking into account  $f$  explicitly, expressed as:

$$519 \quad h_E = C_i \frac{u_*}{N} \quad \text{for all SBL and NBL, (12)}$$

520 where  $C_i$  is an empirical coefficient. Here we select the CN, NS, and LS ABLH dataset, and fit the data with  
 521 the corresponding expressions in Eq. (10–12) to obtain the empirical coefficients, and the results are  
 522 presented in Fig. 12. All three expressions tend to well represent the ABLHs, with significant correlation  
 523 coefficients. The empirical coefficients  $C_N$  and  $C_S$  are 1.7 and 0.4, respectively, which are close to the typical  
 524 values determined through large-eddy simulations (Zilitinkevich, 2012). The coefficient  $C_i = 20$  in Fig. 12c  
 525 is double the typical value of 10 (Vogelezang and Holtslag, 1996), but agrees with the results reported by  
 526 Overland and Davidson (1992) for the ABL over sea ice. The difference in  $C_i$  may be attributed to the unique  
 527 free-flow stability or other potential mechanisms of ABL development in the Arctic atmosphere.

528 In summary, near-surface conditions and free-flow stability play a key role in ABL development and  
 529 are also **indicators**, in that one can roughly determine the development state of the whole ABL from these  
 530 basic variables.

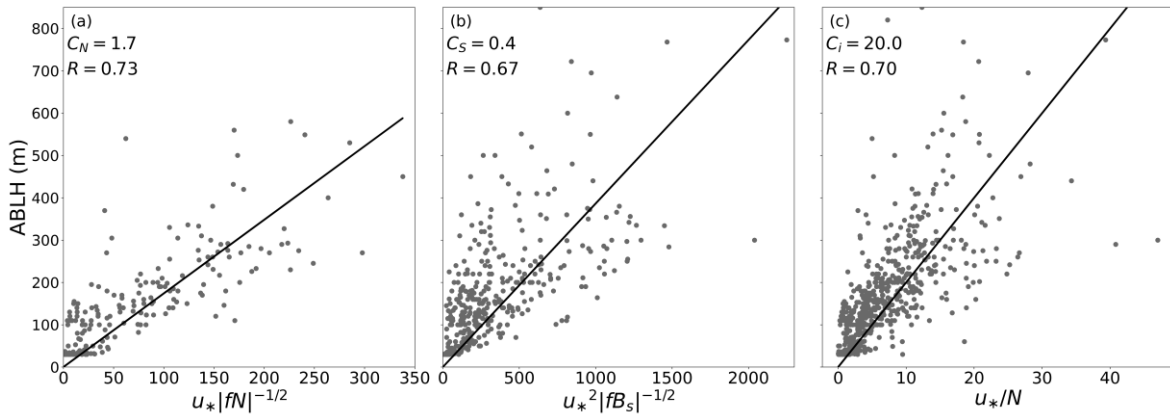
531



532

533 Figure 11 The ABLHs and bin-averaged values for (a) equivalent potential temperature gradient,  $\theta_{Egrad}$  (K),  
 534 (b) friction velocity,  $u_*$  ( $m s^{-1}$ ), and (c) turbulent kinetic energy dissipation rate,  $\epsilon$  ( $m^2 s^{-3}$ ). The average bins  
 535 for  $\theta_{Egrad}$ ,  $u_*$ , and  $\epsilon$  logarithm are 0.2 K, 0.05  $m s^{-1}$ , and 0.5  $m^2 s^{-3}$ , respectively. The correlation coefficient  
 536  $R$  is given in (b), which is statistically significant ( $p < 0.05$ ). The dashed vertical lines indicate the thresholds  
 537 of (a)  $\theta_{Egrad} = 0$  K and (c)  $\epsilon = 5 \times 10^{-5}$   $m^2 s^{-3}$ .

538



539

540 Figure 12 The ABLHs versus three expressions in Eq. (10–12). The empirical coefficients  $C_N$ ,  $C_S$ , and  $C_i$   
 541 are given in (a), (b), and (c), respectively, and represent the slope of the best fit line (black line). The  
 542 correlation coefficient  $R$  is given in each panel, which is statistically significant ( $p < 0.05$ ).

543

#### 544 4.3 Case study #1: Intensively developed ABL 13 April - 24 May 2020

545 To investigate the ABL development and its controlling factors, we analyze the association of the ABLH  
 546 with vertical thermal structure and near-surface conditions during the transition period (see Fig. 7) when the  
 547 ABLH was generally the highest. Figure 13 presents time-height cross sections of  $\theta_E$ , wind speed, and  $RH$ ,  
 548 and the time series of near-surface temperature and surface pressure during this period. We divide the whole  
 549 period into three parts based on the ABLH and the vertical structure of the lower troposphere. Overall, the  
 550 near-surface temperature is generally warmer than  $-20$  °C and shows gradual warming towards the melting

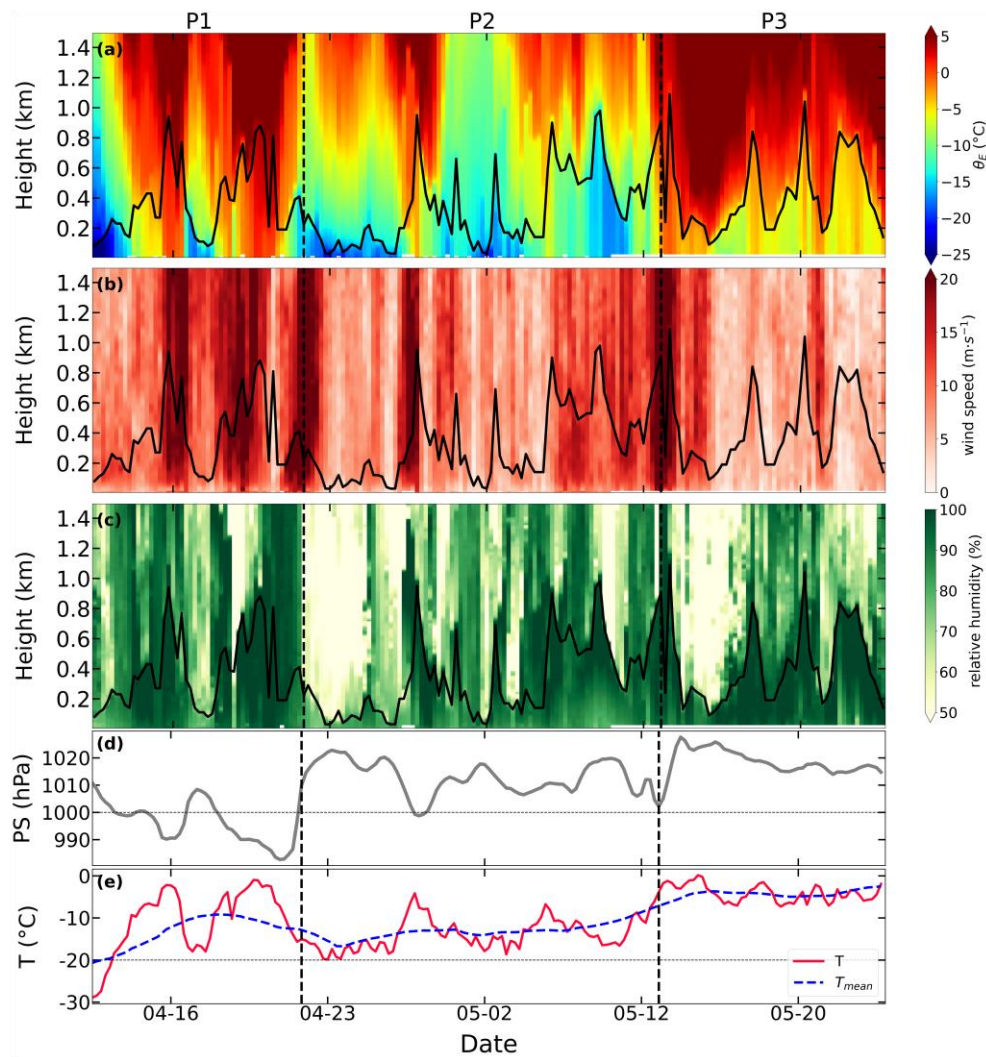
551 point. In Period 1, a warm and moist air advection event affects the measurement area, resulting in increased  
552 air temperature, near-saturated  $RH$ , strong winds throughout the lower troposphere, and low surface pressure.  
553 The approximately constant  $\theta_E$  profile near the surface facilitates exchange between the upper and lower  
554 layers, and the high-speed wind profile enhances mechanical mixing, leading to highly developed ABL and  
555 ABLH exceeding 600 m. In Period 2, the near-surface air temperature drops again to between -20 and -10  
556 °C, which causes a temperature inversion and partially suppresses the ABL development. However, periodic  
557 layers of near-saturated  $RH$  extending up to 600m or more indicate the presence of clouds. The ABLH at  
558 these times is related to the depth of the near-saturated layer, consistent with a structure where the cloud-  
559 induced mixed layer aloft couples with the near-surface mixed layer, forming a deeper ABL and higher  
560 ABLH (Wang et al., 2001; Shupe et al., 2013). In Period 3, a high-pressure synoptic system occurs and  
561 suppresses the development of the ABL, but the cloud-driven turbulent mixing still exists and counteracts  
562 the influence of the high-pressure system. In summary, the development of the ABL mainly depends on  
563 large-scale synoptic processes, especially warm-air advection events. Additionally, the interaction between  
564 the surface-mixed layer and cloud-mixed layer also plays a significant role in the ABL development.

565

566

567





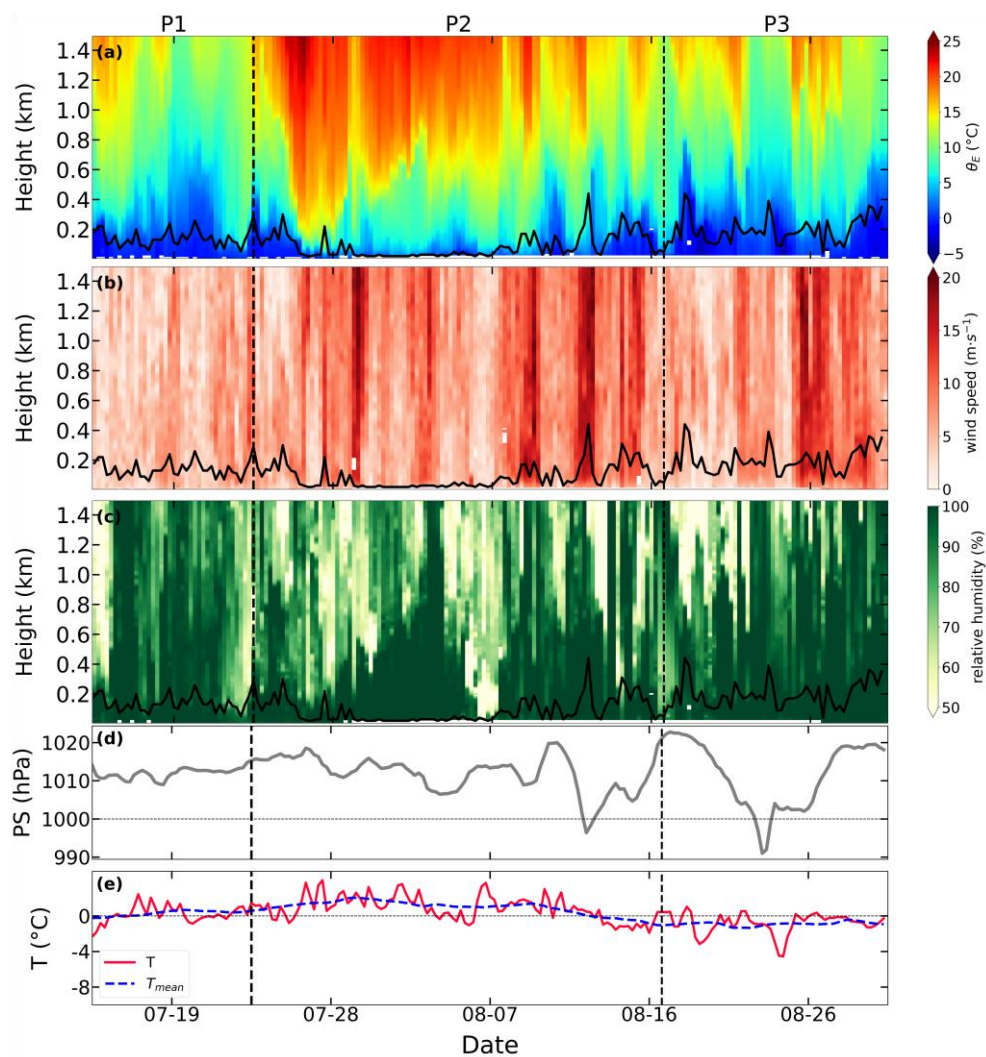
568  
 569 Figure 13 Time-height sections of (a) equivalent potential temperature, (b) horizontal wind speed, and (c)  
 570 relative humidity and time series of (d) surface pressure and (e) near-surface air temperature (red line) and  
 571 7 d running mean of near-surface temperature (blue line). The whole period is from 13 April 2020 to 24 May  
 572 2020. Vertical dashed lines mark the identified periods P1 to P3. The black solid lines in panels (a–c) denote  
 573 the ABLH during this period.

574

#### 575 4.4 Case study #2: the severely suppressed ABL 15 July – 30 August 2020

576 The Arctic ABL is suppressed most of the time, especially in the late summer for more than a month.  
 577 We choose the severely suppressed ABL in this period as a case to analyze the influences of vertical thermal  
 578 structure and near-surface conditions on the ABLH. The results are shown in Fig. 14, and the whole period  
 579 is divided into three parts, similar to Fig. 13. In Period 1, the near-surface air temperature is constrained to  
 580  $\sim 0$  °C due to the melting surface, and the temperature inversion and weak wind are dominant throughout the  
 581 lower troposphere, which suppresses the ABL development. In Period 2, warm-air advection occurs in the  
 582 lower troposphere, strengthening the temperature inversion and contributing to further ABL suppression and  
 583 an ABLH often lower than 100 m. Because of the constrained near-surface temperature, this structure is  
 584 distinct from that of the spring “transition” period when warm-air advection facilitates ABL development.

585 In Period 3, the near-surface and upper-layer temperatures start to decrease, and the temperature inversion  
 586 weakens, which makes the ABLH periodically grow up to  $\sim 400$  m. Despite that, the ABL is still stably  
 587 stratified, and the ample moisture and clouds cannot contribute significantly to the ABL development, which  
 588 is consistent with Shupe et al. (2013). It is important to note that during the second half of Period 2, the  
 589 *Polarstern* transited from near the sea ice edge to near the North Pole, such that this transition towards  
 590 weaker temperature inversions is related to both spatial and seasonal shifts. In summary, the suppression of  
 591 the ABL during the “summer melt” period results from strong temperature inversions and weak winds, and  
 592 cloud-driven turbulent mixing is inhibited from interacting with the surface layer due to the near-surface  
 593 stability. In this period, warm-air advection events enhance the ABL suppression, opposite to the “transition”  
 594 period.



595 Figure 14 Similar to Fig. 13, but the period is from 15 July 2020 to 30 August 2020.

597  
598

### 599 **5 MOSAiC – SHEBA comparison**

600 The MOSAiC and SHEBA observations were both made over the Arctic sea ice during yearlong periods.  
 601 In terms of the location of observation sites, the SHEBA campaign took place in the Beaufort and Chukchi

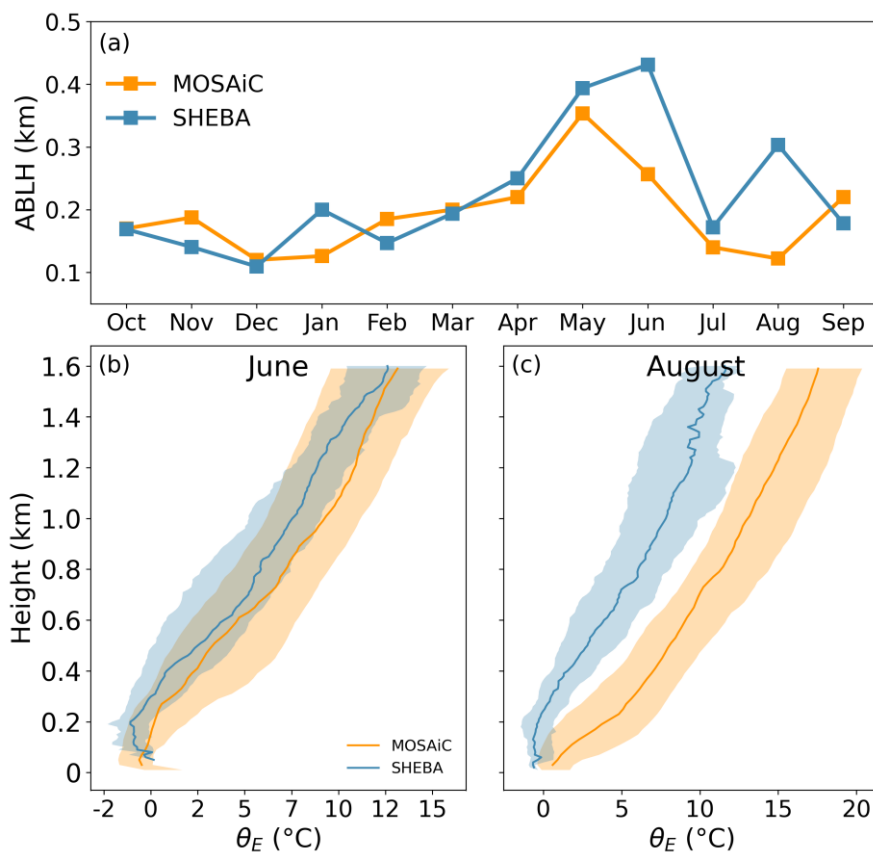


602 Seas (Perovich et al., 2003), while the MOSAiC observations took place along the transpolar drift for much  
603 of the year, in the higher latitudes of the Fram Strait in June, July, and early August, and again near the North  
604 Pole in late August and September. The comparison between the two campaigns could provide insight into  
605 the spatial and temporal variability in the Arctic ABL structure. The monthly ABLHs of the two campaigns  
606 are presented in Fig. 15a. The overall distributions of ABLH are similar during the annual cycle, however,  
607 the SHEBA ABLH is significantly higher than the MOSAiC ABLH in June and August. We will discuss  
608 these differences based on the ABL thermal structure.

609 Comparisons of monthly  $\theta_E$  profiles between the two campaigns during June and August are presented  
610 in Fig. 15 (b, c). It is clear that  $\theta_E$  within the lower troposphere during MOSAiC is much higher than that  
611 during SHEBA, especially in August. In June, the near-surface  $\theta_E$  values in both campaigns are close,  
612 because both were over melting sea ice. However, on average, the upper-layer  $\theta_E$  during SHEBA is lower  
613 than that during MOSAiC, especially at a height of around 200 m, which results in decreased low-level  
614 stability that supports ABL development. This difference explains why the monthly SHEBA ABLH rises  
615 from May to June, but the monthly MOSAiC ABLH decreases at this time. In July at SHEBA, the increased  
616 air temperature in the lower troposphere combined with constrained near-surface  $\theta_E$  results in a significant  
617 temperature inversion that suppresses the ABL development (not shown). Thus, the ABLH values at SHEBA  
618 and MOSAiC are comparable in July. In August, the  $\theta_E$  profiles from the two campaigns are significantly  
619 different. The surface at both locations is still mostly constrained to be near the melting point, while the  
620 lower troposphere at SHEBA starts to cool more than that at MOSAiC. The SHEBA  $\theta_E$  profile exhibits a  
621 near-neutral or convective state, while the MOSAiC  $\theta_E$  profile shows a further enhanced surface temperature  
622 inversion due to warm air advection aloft, which maintains the ABL suppression. To sum up, the increase in  
623 air temperature in the lower troposphere in early summer during MOSAiC precedes that during SHEBA,  
624 while the cooling of the lower troposphere in late summer during MOSAiC lags that during SHEBA. These  
625 are the main factors contributing to the ABLH differences between the two campaigns.

626 The atmospheric warming during the MOSAiC summer may be attributed to ongoing Arctic warming  
627 that contributes a different atmospheric structure, but the impacts of transit periods and different synoptic  
628 backgrounds should also be considered. First, there is the complexity of the transit periods during MOSAiC.  
629 During the first half of June, *Polarstern* travelled northward into a somewhat loosened sea ice pack and  
630 followed open water areas as much as possible. If anything, the higher fraction of open water along this  
631 transit path would promote more heat exchange between the surface and ABL and higher ABLH than the  
632 regional ice pack (e.g., Fig. 7), which suggests that the observed difference between MOSAiC and SHEBA  
633 cannot be explained by this transit period. However, in the first part of August, when *Polarstern* transited  
634 preferentially through open water areas during its movement further north, the transit environment was in a  
635 persistent melting state with warm air advection aloft. It is not clear how this transit ultimately impacted the  
636 monthly ABLH results, although the values during the transit period were lower than those during the final  
637 10 days of August when *Polarstern* was again passively drifting with the sea ice (Figs. 7, 14). Thus, some  
638 of the difference from SHEBA at this time could have been attributed to the specific conditions encountered  
639 during movement of the vessel. Additionally, these two campaigns were in different storm tracks with

640 markedly different types of regional advection patterns. For example, in summer, MOSAiC was approaching  
 641 the Fram Strait where northward warm air advection is common. Thus, synoptic variability likely plays a  
 642 big role in the ABL thermal structure. In summary, there is large variability in the Arctic ABL structure  
 643 during summer caused by the surface melting state, and more detailed assessments are needed to study the  
 644 specific causes for the atmospheric warming and possible influences of changing Arctic conditions on the  
 645 ABL structure.



646  
 647 Figure 15 Comparison of ABL during SHEBA (blue squares, lines, and shadings) and MOSAiC (yellow  
 648 squares, lines, and shadings), including (a) annual cycle of monthly median ABLH and monthly  $\theta_E$  profiles  
 649 in (b) June and (c) August. The solid lines in (b–c) indicate the median profiles, and the shadings indicate  
 650 the range of 25th- and 75th- percentile profiles. The median ABLHs of SHEBA are from Dai et al. (2011).

651  
 652 **6 Conclusions**

653 This study is carried out using merged radiosounding data and corresponding surface meteorological  
 654 observations and cloud properties collected during the MOSAiC expedition over a year-long period. A  
 655 number of ABLH algorithms are first evaluated, prompting us to implement an improved  $Ri$  algorithm that  
 656 takes cloud effects into consideration. We propose a critical  $Ri = 0.35$  and further analyze its value choice  
 657 and stability dependence. Subsequently, we use the manually-labeled ABLH dataset to study how  
 658 atmospheric thermal structure and near-surface conditions impact the characteristics and evolution of the  
 659 ABL during the MOSAiC year. Lastly, we use two cases to explore the mechanisms of ABL development  
 660 and suppression over the Arctic sea-ice surface. The main conclusions are as follows.

661 During the MOSAiC year, the mean ABLH is 231 m, with SBLs, NBLs and CBLs accounting for 43 %,  
662 31 %, and 26 % of the profiles, respectively. The annual cycle of the Arctic ABLH is clearly characterized  
663 by a distinct peak in May and two minima in January and July-August. Low-level clouds significantly  
664 contribute to the Arctic ABL development during the MOSAiC year, except in winter, when low-level clouds  
665 are less frequent. Compared to the SHEBA ABLH, the MOSAiC ABLH is suppressed in June and August,  
666 which is caused by increased atmospheric warming in the MOSAiC ABL during the “summer melt” period  
667 compared to SHEBA.

668 The annual cycle of ABLH over the Arctic Ocean is primarily controlled by the seasonal evolution of  
669 the ABL thermal structure and near-surface meteorological conditions. In the “winter” period, temperature  
670 inversions form due to negative net radiation at the surface and are associated with low ABLHs. In the spring  
671 “transition” period, the rapid increase of near-surface temperature weakens the temperature inversion,  
672 facilitating the development of the ABL. In the “summer melt” period, temperature inversions result from a  
673 fixed surface temperature at the melting point and warm-air advection aloft, which suppresses ABL  
674 development. For near-surface conditions and free-flow stability, a negative  $\theta_{Egrad}$  and large TKE dissipation  
675 rate are characteristic of significant ABL development. In addition, empirical formulas relating ABLH to  
676 friction velocity, near-surface and free-flow stabilities are also tested, and the results suggest that the  
677 MOSAiC ABLH can be roughly estimated based on these basic variables.

678 During MOSAiC, the development of the ABL is irregular, and only occurs during intermittent periods.  
679 The year is characterized by occasions of abrupt growth of the ABLH and intensive ABLH variation for  
680 several days thereafter. These unique features are caused by large-scale synoptic processes (e.g., advection  
681 events) that bring heat, moisture, and clouds. It is worth noting that some large-scale events can have the  
682 opposite effect on the ABL. For example, warm-air advection can facilitate ABL development in the spring  
683 “transition” period but can cause ABL suppression in the “summer melt” period, when the constrained near-  
684 surface temperature cannot respond to the warmth aloft.

685 The findings reported here provide new insight into the annual variability and properties of the ABL  
686 and ABLH over sea ice in the ‘new Arctic’. The ABLH contains information directly related to the thermal  
687 structure of the ABL and includes the impacts of weather events and large-scale circulations on the ABL  
688 structure. The ABL development supported by cloud processes was captured by the improved  $Ri$  algorithm,  
689 which is similar to Brooks et al. (2017). However, the representativity of these results must still be  
690 established by comparing them with additional observations, and the influences of other variables (e.g.,  
691 energy budget terms) on the ABLH should also be considered in future research.

692

### 693 **Data Availability**

694 The radiosonde data are available at the PANGAEA Data Publisher at  
695 <https://doi.org/10.1594/PANGAEA.943870> (Maturilli et al., 2022). All value-added products and surface  
696 meteorological data are available at the archive of the US Department of Energy Atmospheric Radiation  
697 Measurement Program. The Planetary Boundary Layer Height Value-Added Product is available at  
698 <http://dx.doi.org/10.5439/1150253> (Riihimaki et al., 2019). The cloud property data is available at  
699 <https://doi.org/10.5439/1871015> (Shupe, 2022). The MOSAiC surface flux and other meteorological data  
700 are available at the Arctic Data Center at <http://dx.doi.org/10.18739/A2PV6B83F> (Cox et al., 2023). The

701 merged sounding-tower data are available at PANGAEA. The SHEBA-based sounding data are available at  
702 <https://doi.org/10.5065/D6FQ9V0Z> (Moritz, 2017).

703

#### 704 **Author contribution**

705 Shijie Peng: formal analysis; investigation; methodology; visualization; writing-original draft; writing-  
706 review and editing. Qinghua Yang: conceptualization; formal analysis; project administration; writing-  
707 review and editing; funding acquisition; supervision. Matthew D. Shupe: data curation; formal analysis;  
708 validation; resources; writing-review and editing. Xingya Xi: methodology; validation; writing-review and  
709 editing. Bo Han: formal analysis; validation; writing-review and editing. Dake Chen: formal analysis;  
710 validation; writing-review and editing; supervision. Sandro Dahlke: data curation; validation; writing-review  
711 and editing; Changwei Liu: data curation; formal analysis; validation; visualization; writing-original draft;  
712 writing-review and editing.

713

#### 714 **Competing interests**

715 None.

716

#### 717 **Acknowledgments**

718 Data used in this manuscript were produced as part of the international Multidisciplinary drifting  
719 Observatory for the Study of Arctic Climate (MOSAiC) expedition with tag MOSAiC20192020. We thank  
720 all persons involved in the expedition of the Research Vessel Polarstern during MOSAiC in 2019-2020  
721 (AWI\_PS122\_00) as listed in Nixdorf et al. (2021). A subset of data was obtained from the Atmospheric  
722 Radiation Measurement (ARM) User Facility, a US Department of Energy (DOE) Office of Science User  
723 Facility Managed by the Biological and Environmental Research Program. The Alfred Wegener Institute,  
724 DOE ARM Program, and German Weather Service are acknowledged for their contributions to the MOSAiC  
725 sounding program.

726

#### 727 **Financial Support**

728 This study is supported by the National Natural Science Foundation of China (Nos. 42105072, 41922044,  
729 41941009), the Guangdong Basic and Applied Basic Research Foundation (Nos. 2021A1515012209,  
730 2020B1515020025), and the China Postdoctoral Science Foundation (Nos. 2021M693585). MDS was  
731 supported by the US National Science Foundation (OPP-1724551), the DOE Atmospheric System Research  
732 Program (DE-SC0019251, DE-SC0023036), and the National Oceanic and Atmospheric Administration  
733 Global Ocean Monitoring and Observing program (FundRef <https://doi.org/10.13039/100018302>,  
734 NA22OAR4320151).

735

736

#### 737 **References**

738 Akansu, E. F., Dahlke, S., Siebert, H., and Wendisch, M.: Determining the surface mixing layer height of  
739 the Arctic atmospheric boundary layer during polar night in cloudless and cloudy conditions,  
740 EGU sphere [preprint], <https://doi.org/10.5194/egusphere-2023-629>, 2023.

741 Andreas, E. L., Claffy, K. J., and Makshtas, A. P.: Low-level atmospheric jets and inversions over the  
742 western Weddell Sea, *Boundary-Layer Meteorol.*, 97, 459-486,  
743 <https://doi.org/10.1023/A:1002793831076>, 2000.

744 Banta, R. M., Pichugina, Y. L., and Newsom, R. K.: Relationship between low-level jet properties and  
745 turbulence kinetic energy in the nocturnal stable boundary layer, *J. Atmos. Sci.*, 60, 2549-2555,  
746 [https://doi.org/10.1175/1520-0469\(2003\)060<2549:RBLJPA>2.0.CO;2](https://doi.org/10.1175/1520-0469(2003)060<2549:RBLJPA>2.0.CO;2), 2003.

747 Barten, J. G. M., Ganzeveld, L. N., Steeneveld, G. J., Blomquist, B. W., Angot, H., Archer, S. D., Bariteau,  
748 L., Beck, I., Boyer, M., von der Gathen, P., Helmig, D., Howard, D., Hueber, J., Jacobi, H.-W., Jokinen,  
749 T., Laurila, T., Posman, K. M., Quéléver, L., Schmale, J., Shupe, M. D., and Krol, M. C.: Low ozone  
750 dry deposition rates to sea ice during the MOSAiC field campaign: Implications for the Arctic boundary  
751 layer ozone budget, *Elementa: Sci. Anthropol.*, 11, 00086, <https://doi.org/10.1525/elementa.2022.00086>,

752 2023.

753 Basu, S., Holtslag, A. A. M., Caporaso, L., Riccio, A., and Steeneveld, G. J.: Observational Support for the  
754 Stability Dependence of the Bulk Richardson Number Across the Stable Boundary Layer. *Boundary-*  
755 *Layer Meteorol.* 150, 515–523, <https://doi.org/10.1007/s10546-013-9878-y>, 2014.

756 Basu, S, Holtslag, A. A. M., van de Wiel, B. J. H., Moene, A. F., and Steeneveld, G. J.: An inconvenient  
757 “truth” about using sensible heat flux as a surface boundary condition in models under stably stratified  
758 regimes. *Acta Geophys.*, 56, 88–99, <https://doi.org/10.2478/s11600-007-0038-y>, 2008.

759 Blunden, J. and Arndt, D. S.: A Look at 2018: Takeaway Points from the State of the Climate Supplement,  
760 *Bull. Amer. Meteorol. Soc.*, 100, 1625-1636, <https://doi.org/10.1175/bams-d-19-0193.1>, 2019.

761 Brooks, I. M., Tjernström, M., Persson, P. O. G., Shupe, M. D., Atkinson, R. A., Canut, G., Birch, C. E.,  
762 Mauritsen, T., Sedlar, J., and Brooks, B. J.: The Turbulent Structure of the Arctic Summer Boundary  
763 Layer During The Arctic Summer Cloud-Ocean Study, *J. Geophys. Res.-Atmos.*, 122, 9685-9704,  
764 <https://doi.org/10.1002/2017jd027234>, 2017.

765 Busch, N., Ebel, U., Kraus, H., and Schaller, E.: The structure of the subpolar inversion-capped ABL,  
766 *Archives for meteorology, geophysics, and bioclimatology, Series A*, 31, 1-18,  
767 <https://doi.org/10.1007/BF02257738>, 1982.

768 Cox, C., Gallagher, M., Shupe, M., Persson, O., Blomquist, B., Grachev, A., Riihimaki, L., Kutchenreiter,  
769 M., Morris, V., Solomon, A., Brooks, I., Costa, D., Gottas, D., Hutchings, J., Osborn, J., Morris, S.,  
770 Preusser, A., Uttal, T.: Met City meteorological and surface flux measurements (Level 3 Final),  
771 Multidisciplinary drifting Observatory for the Study of Arctic Climate (MOSAiC), central Arctic,  
772 October 2019 - September 2020 [data set], <https://doi.org/10.18739/A2PV6B83F>, 2023.

773 Dai, C., Gao, Z., Wang, Q., and Cheng, G.: Analysis of Atmospheric Boundary Layer Height Characteristics  
774 over the Arctic Ocean Using the Aircraft and GPS Soundings, *Atmospheric Ocean. Sci.*, 4, 124-130,  
775 <https://doi.org/10.1080/16742834.2011.11446916>, 2011.

776 Dai, C., Wang, Q., Kalogiros, J. A., Lenschow, D. H., Gao, Z., and Zhou, M.: Determining Boundary-Layer  
777 Height from Aircraft Measurements, *Boundary-Layer Meteorol.*, 152, 277-302,  
778 <https://doi.org/10.1007/s10546-014-9929-z>, 2014.

779 Davy, R. and Esau, I.: Differences in the efficacy of climate forcings explained by variations in atmospheric  
780 boundary layer depth, *Nat. Commun.*, 7, 11690, <https://doi.org/10.1175/BAMS-D-11-00187.1>, 2013.

781 Esau, I., Pettersson, L. H., Cancet, M., Chapron, B., Chernokulsky, A., Donlon, C., Sizov, O., Soromotin,  
782 A., and Johannesen, J. A.: The Arctic Amplification and Its Impact: A Synthesis through Satellite  
783 Observations, *Remote Sens.*, 15, 1354, <https://doi.org/10.3390/rs15051354>, 2023.

784 Francis, J. A. and Hunter, E.: New insight into the disappearing Arctic sea ice, *EOS Trans. Am. Geophys.*  
785 *Union*, 87, 509-511, <https://doi.org/10.1029/2006EO460001>, 2006.

786 Graversen, R. G., Mauritsen, T., Tjernström, M., Kallen, E., and Svensson, G.: Vertical structure of recent  
787 Arctic warming, *Nature*, 451, 53-U54, <https://doi.org/10.1038/nature06502>, 2008.

788 Heffter, J. L.: Transport layer depth calculations., *Second Joint Conference on Applications of Air Pollution*  
789 *Meteorology*, 1980.

790 Holtslag, A.A.M., Svensson, G., Baas, P., Basu, S., Beare, B., Beljaars, A.C.M., Bosveld, F.C., Cuxart, J.,  
791 Lindvall, J., Steeneveld, G.J., Tjernström, M. and Van De Wiel, B.J.H.: Stable atmospheric boundary  
792 layers and diurnal cycles: Challenges for weather and climate models, *Bull. Amer. Meteorol. Soc.*, 94,  
793 1691–1706, <https://doi.org/10.1038/ncomms11690>, 2013.

794 Jozef, G., Cassano, J., Dahlke, S., and de Boer, G.: Testing the efficacy of atmospheric boundary layer height  
795 detection algorithms using uncrewed aircraft system data from MOSAiC, *Atmos. Meas. Tech.*, 15,  
796 4001-4022, <https://doi.org/10.5194/amt-15-4001-2022>, 2022.

797 Jozef, G. C., Cassano, J. J., Dahlke, S., Dice, M., Cox, C. J., and de Boer, G.: An Overview of the Vertical  
798 Structure of the Atmospheric Boundary Layer in the Central Arctic during MOSAiC, *EGUsphere*  
799 [preprint], <https://doi.org/10.5194/egusphere-2023-780>, 2023.

800 Kim, J. and Mahrt, L.: Simple Formulation of Turbulent Mixing in the Stable Free Atmosphere and

801 Nocturnal Boundary Layer, *Tellus*, 44A, 381-39, <https://doi.org/10.3402/tellusa.v44i5.14969>, 1992.

802 Kljun, N., Calanca, P., Rotach, M. W., and Schmid, H. P.: The simple two-dimensional parameterisation for  
803 Flux Footprint Predictions (FFP), *Geosci. Model Dev.*, 8(8), 6757–6808, [https://doi.org/10.5194/gmd-](https://doi.org/10.5194/gmd-8-3695-2015)  
804 8-3695-2015, 2015.

805 Knudsen, E. M., Heinold, B., Dahlke, S., Bozem, H., Crewell, S., Gorodetskaya, I. V., Heygster, G., Kunkel,  
806 D., Maturilli, M., Mech, M., Viceto, C., Rinke, A., Schmithusen, H., Ehrlich, A., Macke, A., Luepkes,  
807 C., and Wendisch, M.: Meteorological conditions during the ACLOUD/PASCAL field campaign near  
808 Svalbard in early summer 2017, *Atmospheric Chem. Phys.*, 18, 17995-18022,  
809 <https://doi.org/10.5194/acp-18-17995-2018>, 2018.

810 Knust, R.: Polar Research and Supply Vessel POLARSTERN operated by the Alfred-Wegener-Institute,  
811 *Journal of large-scale research facilities JLSRF*, 3, <https://doi.org/10.17815/jlsrf-3-163>, 2017.

812 Konor, C. S., Boezio, G. C., Mechoso, C. R., and Arakawa, A.: Parameterization of PBL Processes in an  
813 Atmospheric General Circulation Model: Description and Preliminary Assessment, *Mon. Weather Rev.*,  
814 137, 1061-1082, <https://doi.org/10.1175/2008mwr2464.1>, 2009.

815 Landrum, L. and Holland, M. M.: Extremes become routine in an emerging new Arctic, *Nature Clim. Change*,  
816 10, 1108-1115, <https://doi.org/10.1038/s41558-020-0892-z>, 2020.

817 Lenschow D. H., Zhou M., Zeng X., Chen L., and Xu X.: Measurements of fine-scale structure at the top of  
818 marine stratocumulus, *Boundary-Layer Meteorol.*, 97:331–357,  
819 <https://doi.org/10.1023/A:1002780019748>, 2000.

820 Liu, S. and Liang, X.: Observed Diurnal Cycle Climatology of Planetary Boundary Layer Height, *J. Clim.*,  
821 23, 5790-5809, <https://doi.org/10.1175/2010jcli3552.1>, 2010.

822 Mahrt, L.: Modelling the depth of the stable boundary-layer, *Boundary-Layer Meteorol.*, 21, 3-19,  
823 <https://doi.org/10.1007/BF00119363>, 1981.

824 Mahrt, L.: Stably stratified atmospheric boundary layers, *Annu. Rev. Fluid Mech.*, 46, 23–45,  
825 <https://doi.org/10.1146/annurev-fluid-010313-141354>, 2014.

826 Mahrt L., Heald R. C., Lenschow D. H., Stankov B. B., and Troen I. B.: An observational study of the  
827 structure of the nocturnal boundary layer, *Boundary-Layer Meteorol.*, 17:247–264,  
828 <https://doi.org/10.1007/BF00117983>, 1979.

829 Marsik, F. J., Fischer, K. W., McDonald, T. D., and Samson, P. J.: Comparison of Methods for Estimating  
830 Mixing Height Used during the 1992 Atlanta Field Intensive, *J. Appl. Meteorol. Climatol.*, 34, 1802-  
831 1814, [https://doi.org/10.1175/1520-0450\(1995\)034<1802:Comfem>2.0.Co;2](https://doi.org/10.1175/1520-0450(1995)034<1802:Comfem>2.0.Co;2), 1995.

832 Martucci G, Matthey R, and Mitev V.: Comparison between backscatter lidar and radiosonde measurements  
833 of the diurnal and nocturnal stratification in the lower troposphere, *J. Atmos. Oceanic Technol.*,  
834 24:1231–1244, <https://doi.org/10.1175/JTECH2036.1>, 2007.

835 Maturilli, M., Sommer, M., Holdridge, D. J., Dahlke, S., Graeser, J., Sommerfeld, A., Jaiser, R., Deckelmann,  
836 H., and Schulz, A.: MOSAiC radiosonde data (level 3) [data set],  
837 <https://doi.org/10.1594/PANGAEA.943870>, 2022.

838 Matveeva, T. A. and Semenov, V. A.: Regional Features of the Arctic Sea Ice Area Changes in 2000–2019  
839 versus 1979–1999 Periods, *Atmosphere*, 13, 1434. <https://doi.org/10.3390/atmos1309143>, 2022.

840 Meier, W. N., and Stroeve, J.: An updated assessment of the changing Arctic sea ice cover, *Oceanography*,  
841 35(3–4): 10–19, <https://doi.org/10.5670/oceanog.2022.114>, 2022.

842 Moritz, R.: Soundings, Ice Camp NCAR/GLAS raobs. (ASCII). Version 2.0., University of Washington,  
843 UCAR/NCAR - Earth Observing Laboratory [data set], <https://doi.org/10.5065/D6FQ9V0Z>, 2017.

844 Nixdorf, U., Dethloff, K., Rex, M., Shupe, M., Sommerfeld, A., Perovich, D. K., Nicolaus, M., Heuze, C.,  
845 Rabe, B., Loose, B., Damm, E., Gradinger, R., Fong, A., Maslowski, W., Rinke, A., Kwok, R., Spreen,  
846 G., Wendisch, M., Herber, A., Hirsekorn, M., Mohaupt, V., Frickenhaus, S., Immerz, A., Weiss-Tuider,  
847 K., Koenig, B., Menedoht, D., Regnery, J., Gerchow, P., Ransby, D., Krumpfen, T., Morgenstern, A.,  
848 Haas, C., Kanzow, T., Rack, F., Saitzev, V., Sokolov, V., Makarov, A., Schwarze, S., Wunderlick, T.,  
849 Wurr, K., Boetius, A.: MOSAiC extended acknowledgement., Zenodo.,

850 <http://dx.doi.org/10.5281/zenodo.5541624>, 2021.

851 Overland, J. E., Dunlea, E. J., Box, J. E., Corell, R. W., Forsius, M., Kattsov, V. M., Olsen, M. S., Pawlak,  
852 J., Reiersen, L. O., and Wang, M.: The urgency of Arctic change, *Polar Sci.*, 21, 6-13,  
853 <https://doi.org/10.1016/j.polar.2018.11.008>, 2019.

854 Palo, T., Vihma, T., Jaagus, J., and Jakobson, E.: Observations of temperature inversions over central Arctic  
855 sea ice in summer, *Q. J. R. Meteorol. Soc.*, 143, 2741-2754, <https://doi.org/10.1002/qj.3123>, 2017.

856 Perovich, D. K., Grenfell, T. C., Richter-Menge, J. A., Light, B., Tucker III, W. B., and Eicken, H.: Thin  
857 and thinner: Sea ice mass balance measurements during SHEBA, *J. Geophys. Res.-Oceans*, 108,  
858 <https://doi.org/10.1029/2001JC001079>, 2003.

859 Persson, P. O. G., Fairall, C. W., Andreas, E. L., Guest, P. S., and Perovich, D. K.: Measurements near the  
860 Atmospheric Surface Flux Group tower at SHEBA: Near-surface conditions and surface energy budget,  
861 *J. Geophys. Res.-Oceans*, 107, 35, <https://doi.org/10.1029/2000jc000705>, 2002.

862 Pollard R. T., Rhines P.B., and Thompson R.: The deepening of the wind-mixed layer, *Geophys. Fluid Dyn.*,  
863 3, 381–404, <https://doi.org/10.1080/03091927208236105>, 1973.

864 Richardson, H., Basu, S., and Holtslag, A. A. M.: Improving Stable Boundary-Layer Height Estimation  
865 Using a Stability-Dependent Critical Bulk Richardson Number, *Boundary-Layer Meteorol.*, 148, 93-  
866 109, <https://doi.org/10.1007/s10546-013-9812-3>, 2013.

867 Riihimaki, L., Sivaraman, C., and Zhang, D.: Planetary Boundary Layer Height  
868 (PBLHTSONDE1MCFARL), Atmospheric Radiation Measurement (ARM) User Facility [data set],  
869 <https://doi.org/10.5439/1150253>, 2019.

870 Seibert, P., Beyrich, F., Gryning, S. E., Joffre, S., Rasmussen, A., and Tercier, P.: Review and  
871 intercomparison of operational methods for the determination of the mixing height, *Atmos. Environ.*,  
872 34, 1001-1027, [https://doi.org/10.1016/s1352-2310\(99\)00349-0](https://doi.org/10.1016/s1352-2310(99)00349-0), 2000.

873 Seidel, D. J., Ao, C. O., and Li, K.: Estimating climatological planetary boundary layer heights from  
874 radiosonde observations: Comparison of methods and uncertainty analysis, *J. Geophys. Res.-Atmos.*,  
875 115, <https://doi.org/10.1029/2009JD013680>, 2010.

876 Seidel, D. J., Zhang, Y. H., Beljaars, A., Golaz, J. C., Jacobson, A. R., and Medeiros, B.: Climatology of the  
877 planetary boundary layer over the continental United States and Europe, *J. Geophys. Res.-Atmos.*, 117,  
878 15, <https://doi.org/10.1029/2012jd018143>, 2012.

879 Shupe, M. D.: ShupeTurner cloud microphysics product, ARM Mobile Facility (MOS) MOSAiC  
880 (Drifting Obs – Study of Arctic Climate) [data set], <https://doi.org/10.5439/1871015>, 2022.

881 Shupe, M. D., and Intrieri, J. M.: Cloud radiative forcing of the Arctic surface: The influence of cloud  
882 properties, surface albedo, and solar zenith angle, *J. Climate*, 17, 616–628,  
883 [https://doi.org/10.1175/1520-0442\(2004\)017<0616:CRFOTA>2.0.CO;2](https://doi.org/10.1175/1520-0442(2004)017<0616:CRFOTA>2.0.CO;2), 2004.

884 Shupe, M. D., Walden, V. P., Eloranta, E., Uttal, T., Campbell, J. R., Starkweather, S. M., and Shiobara, M.:  
885 Clouds at Arctic Atmospheric Observatories. Part I: Occurrence and Macrophysical Properties, *J. Appl.*  
886 *Meteorol. Clim.*, 50, 626-644, <https://doi.org/10.1175/2010JAMC2467.1>, 2011.

887 Shupe, M. D., Persson, P. O. G., Brooks, I. M., Tjernström, M., Sedlar, J., Mauritsen, T., Sjogren, S., and  
888 Leck, C.: Cloud and boundary layer interactions over the Arctic sea ice in late summer, *Atmos. Chem.*  
889 *Phys.*, 13, 9379-9399, <https://doi.org/10.5194/acp-13-9379-2013>, 2013.

890 Shupe, M. D., Rex, M., Blomquist, B., Persson, P. O. G., Schmale, J., Uttal, T., Althausen, D., Angot, H.,  
891 Archer, S., Bariteau, L., Beck, I., Bilberry, J., Bucci, S., Buck, C., Boyer, M., Brasseur, Z., Brooks, I.  
892 M., Calmer, R., Cassano, J., Castro, V., Chu, D., Costa, D., Cox, C. J., Creamean, J., Crewell, S., Dahlke,  
893 S., Damm, E., de Boer, G., Deckelmann, H., Dethloff, K., Dütsch, M., Ebell, K., Ehrlich, A., Ellis, J.,  
894 Engelmann, R., Fong, A. A., Frey, M. M., Gallagher, M. R., Ganzeveld, L., Gradinger, R., Graeser, J.,  
895 Greenamyre, V., Griesche, H., Griffiths, S., Hamilton, J., Heinemann, G., Helmig, D., Herber, A.,  
896 Heuzé, C., Hofer, J., Houchens, T., Howard, D., Inoue, J., Jacobi, H.-W., Jaiser, R., Jokinen, T., Jourdan,  
897 O., Jozef, G., King, W., Kirchgaessner, A., Klingebiel, M., Krassovski, M., Krumpfen, T., Lampert, A.,  
898 Landing, W., Laurila, T., Lawrence, D., Lonardi, M., Loose, B., Lüpkes, C., Maahn, M., Macke, A.,  
899 Maslowski, W., Marsay, C., Maturilli, M., Mech, M., Morris, S., Moser, M., Nicolaus, M., Ortega, P.,

900 Osborn, J., Pätzold, F., Perovich, D. K., Petäjä, T., Pilz, C., Pirazzini, R., Posman, K., Powers, H., Pratt,  
901 K. A., Preußner, A., Quéléver, L., Radenz, M., Rabe, B., Rinke, A., Sachs, T., Schulz, A., Siebert, H.,  
902 Silva, T., Solomon, A., Sommerfeld, A., Spreen, G., Stephens, M., Stohl, A., Svensson, G., Uin, J.,  
903 Viegas, J., Voigt, C., von der Gathen, P., Wehner, B., Welker, J. M., Wendisch, M., Werner, M., Xie,  
904 Z., and Yue, F.: Overview of the MOSAiC expedition—Atmosphere, *Elementa: Sci. Anthropol.*, 10,  
905 <https://doi.org/10.1525/elementa.2021.00060>, 2022.

906 Shupe, M. D., Turner, D. D., Zwink, A., Theiman, M. M., Mlawer, M. J., and Shippert T. R.: Deriving  
907 Arctic cloud microphysics at Barrow: Algorithms, results, and radiative closure, *J. Appl. Meteor. Clim.*,  
908 54, 1675-1689, doi:10.1175/JAMC-D-15-0054.1, 2015.

909 Silber, I. and Shupe, M. D.: Insights on sources and formation mechanisms of liquid-bearing clouds over  
910 MOSAiC examined from a Lagrangian framework, *Elementa: Sci. Anthropol.*, 10, 000071,  
911 <https://doi.org/10.1525/elementa.2021.000071>, 2022

912 Sivaraman, C., McFarlane, S., Chapman, E., Jensen, M., Toto, T., Liu, S., and Fischer, M.: Planetary  
913 Boundary Layer Height (PBL) Value Added Product (VAP): Radiosonde Retrievals, University of  
914 Maryland, United States, DOE/SC-ARM/TR-132, <https://doi.org/10.2172/1808688>, 2013.

915 Snyder, B. J. and Strawbridge, K. B.: Meteorological analysis of the Pacific 2001 air quality field study,  
916 *Atmos. Environ.*, 38, 5733-5743, <https://doi.org/10.1016/j.atmosenv.2004.02.068>, 2004.

917 Solomon, A., Shupe, M. D., Persson, P. O. G., and Morrison, H.: Moisture and dynamical interactions  
918 maintaining decoupled Arctic mixed-phase stratocumulus in the presence of a humidity inversion,  
919 *Atmos. Chem. Phys.*, 11, 10127-10148, <https://doi.org/10.5194/acp-11-10127-2011>, 2011.

920 Sørensen, J. H., Rasmussen, A., Ellermann, T., and Lyck, E.: Mesoscale influence on long-range transport  
921 — evidence from ETEX modelling and observations, *Atmos. Environ.*, 32, 4207-4217,  
922 [https://doi.org/10.1016/S1352-2310\(98\)00183-6](https://doi.org/10.1016/S1352-2310(98)00183-6), 1998.

923 Sotiropoulou, G., Sedlar, J., Tjernström, M., Shupe, M. D., Brooks, I. M., and Persson, P. O. G.: The  
924 thermodynamic structure of summer Arctic stratocumulus and the dynamic coupling to the surface,  
925 *Atmos. Chem. Phys.*, 14, 12573-12592, <https://doi.org/10.5194/acp-14-12573-2014>, 2014.

926 Steeneveld, G. J., van de Wiel, B. J. H., and Holtslag, A. A. M.: Comments on deriving the equilibrium  
927 height of the stable boundary layer, *Q. J. R. Meteorol. Soc.*, 133, 261-264, <https://doi.org/10.1002/qj.26>,  
928 2007a.

929 Steeneveld, G. J., van de Wiel, B. J. H., and Holtslag, A. A. M.: Diagnostic Equations for the Stable  
930 Boundary Layer Height: Evaluation and Dimensional Analysis, *J. Appl. Meteor. Climatol.*, 46, 212-  
931 225, <https://doi.org/10.1175/JAM2454.1>, 2007b.

932 Sterk, H. A. M., Steeneveld G. J., and Holtslag A. A. M.: The role of snow-surface coupling, radiation, and  
933 turbulent mixing in modeling a stable boundary layer over Arctic sea ice, *J. Geophys. Res.-Atmos.*, 118,  
934 1199– 1217, <https://doi.org/10.1002/jgrd.50158>, 2014.

935 Tjernström, M., Balsley, B. B., Svensson, G., and Nappo, C. J.: The Effects of Critical Layers on Residual  
936 Layer Turbulence, *J. Atmos. Sci.*, 66, 468-480, <https://doi.org/10.1175/2008jas2729.1>, 2009.

937 Tjernström, M., Birch, C. E., Brooks, I. M., Shupe, M. D., Persson, P. O. G., Sedlar, J., Mauritsen, T., Leck,  
938 C., Paatero, J., Szczodrak, M., and Wheeler, C. R.: Meteorological conditions in the central Arctic  
939 summer during the Arctic Summer Cloud Ocean Study (ASCOS), *Atmos. Chem. and Phys.*, 12, 6863-  
940 6889, <https://doi.org/10.5194/acp-12-6863-2012>, 2012.

941 Tjernström, M. and Graverson, R. G.: The vertical structure of the lower Arctic troposphere analysed from  
942 observations and the ERA-40 reanalysis, *Q. J. R. Meteorol. Soc.*, 135, 431-443,  
943 <https://doi.org/10.1002/qj.380>, 2009.

944 Uttal, T., Curry, J. A., McPhee, M. G., Perovich, D. K., Moritz, R. E., Maslanik, J. A., Guest, P. S., Stern,  
945 H. L., Moore, J. A., Turenne, R., Heiberg, A., Serreze, M. C., Wylie, D. P., Persson, O. G., Paulson, C.  
946 A., Halle, C., Morison, J. H., Wheeler, P. A., Makshtas, A., Welch, H., Shupe, M. D., Intrieri, J. M.,  
947 Starnes, K., Lindsey, R. W., Pinkel, R., Pegau, W. S., Stanton, T. P., and Grenfeld, T. C.: Surface Heat  
948 Budget of the Arctic Ocean, *Bull. Amer. Meteorol. Soc.*, 83, 255-276, [https://doi.org/10.1175/1520-0477\(2002\)083<0255:Shbota>2.3.Co;2](https://doi.org/10.1175/1520-0477(2002)083<0255:Shbota>2.3.Co;2), 2002.



950 Vihma, T.: Effects of Arctic Sea Ice Decline on Weather and Climate: A Review, *Surv. Geophys.*, 35, 1175-  
951 1214, <https://doi.org/10.1007/s10712-014-9284-0>, 2014.

952 Vihma, T., Kilpelainen, T., Manninen, M., Sjoblom, A., Jakobson, E., Palo, T., Jaagus, J., and Maturilli, M.:  
953 Characteristics of Temperature and Humidity Inversions and Low-Level Jets over Svalbard Fjords in  
954 Spring, *Adv. Meteorol.*, 2011, 14, <https://doi.org/10.1155/2011/486807>, 2011.

955 Vogelesang, D. H. P. and Holtslag, A. A. M.: Evaluation and model impacts of alternative boundary-layer  
956 height formulations, *Boundary-Layer Meteorol.*, 81, 245-269, <https://doi.org/10.1007/BF02430331>,  
957 1996.

958 Vullers, J., Achtert, P., Brooks, I. M., Tjernström, M., Prytherch, J., Burzik, A., and Neely, R.:  
959 Meteorological and cloud conditions during the Arctic Ocean 2018 expedition, *Atmos. Chem. and Phys.*,  
960 21, 289-314, <https://doi.org/10.5194/acp-21-289-2021>, 2021.

961 Wang, S., Wang, Q., Jordan, R. E., and Persson, P. O. G.: Interactions among longwave radiation of clouds,  
962 turbulence, and snow surface temperature in the Arctic: A model sensitivity study, *J. Geophys. Res.-*  
963 *Atmos.*, 106, 15323-15333, <https://doi.org/10.1029/2000JD900358>, 2001.

964 Wetzel, C. and Bruemmer, B.: An Arctic inversion climatology based on the European Centre Reanalysis  
965 ERA-40, *Meteorologische Zeitschrift*, 20, 589-600, <https://doi.org/10.1127/0941-2948/2011/0295>,  
966 2011.

967 Zhang, J. A., Rogers, R. F., Nolan, D. S., and Marks, F. D.: On the Characteristic Height Scales of the  
968 Hurricane Boundary Layer, *Mon. Weather Rev.*, 139, 2523-2535, <https://doi.org/10.1175/mwr-d-10-05017.1>, 2011.

970 Zhang, Y., Gao, Z., Li, D., Li, Y., Zhang, N., Zhao, X., and Chen, J.: On the computation of planetary  
971 boundary-layer height using the bulk Richardson number method, *Geosci. Model Dev.*, 7, 2599-2611,  
972 <https://doi.org/10.5194/gmd-7-2599-2014>, 2014.

973 Zhang, Y. J., Sun, K., Gao Z. Q., Pan Z. T., Shook M. A., and Li D.: Diurnal Climatology of Planetary  
974 Boundary Layer Height Over the Contiguous United States Derived From AMDAR and Reanalysis  
975 Data, *J. Geophys. Res. Atmos.*, 125, <https://doi.org/10.1029/2020JD032803>, 2020.

976 Zilitinkevich, S. S.: On the determination of the height of the Ekman boundary layer, *Boundary-Layer*  
977 *Meteorol.*, 3, 141–145, <https://doi.org/10.1007/BF02033914>, 1972.

978 Zilitinkevich, S. S.: Third-order transport due to internal waves and non-local turbulence in the stably  
979 stratified surface layer, *Q. J. R. Meteorol. Soc.*, 128, 913–925,  
980 <https://doi.org/10.1256/0035900021643746>, 2002.

981 Zilitinkevich, S. S.: The height of the atmospheric planetary boundary layer: State of the art and new  
982 development, In H. J. S. Fernando, Z. Klaić, & J. McCulley (Eds.), *National Security and Human Health*  
983 *Implications of Climate Change (NATO Science for Peace and Security Series C: Environmental*  
984 *Security)* (pp. 147–161), Dordrecht: Springer. [https://doi.org/10.1007/978-94-007-2430-3\\_13](https://doi.org/10.1007/978-94-007-2430-3_13), 2012.

985 Zilitinkevich, S. S. and Baklanov, A.: Calculation Of The Height Of The Stable Boundary Layer In Practical  
986 Applications, *Boundary-Layer Meteorol.*, 105, 389–409, <https://doi.org/10.1023/A:1020376832738>,  
987 2002.

988 Zilitinkevich, S. S., Elperin, T., Kleorin, N., and Rogachevskii, I.: Energy- and flux-budget (EFB)  
989 turbulence closure model for stably stratified flows. Part I: steady-state, homogeneous regimes.  
990 *Boundary-Layer Meteorol.*, 125, 167–191, <https://doi.org/10.1007/s10546-007-9189-2>, 2007.

991 Zilitinkevich, S. S. and Esau, I. N.: On Integral Measures Of The Neutral Barotropic Planetary Boundary  
992 Layer, *Boundary-Layer Meteorol.*, 104, 371–379. <https://doi.org/10.1023/A:1016540808958>, 2002.

993 Zilitinkevich, S. S. and Esau I. N.: The effect of baroclinicity on the depth of neutral and stable planetary  
994 boundary layers, *Q. J. R. Meteorol. Soc.*, 129, 3339–3356, <https://doi.org/10.1256/qj.02.94>, 2003  
995  
996